Hindawi
Advances in Civil Engineering
Volume 2019, Article ID 7594132, 22 pages
https://doi.org/10.1155/2019/7594132

Research Article

Experimental and Numerical Analysis of the Bolt Connections in a Low-Rise Precast Wall Panel Structure System

Wei Guo,[1,2,3] **Zhipeng Zhai**,[1,2,3] **Zhiwu Yu**,[1,2,3] **Feng Chen**,[1,2,3] **Yongzhi Gong**,[1,2,3] **and Tao Tan**[1]

[1]*School of Civil Engineering, Central South University, Changsha 410075, China*
[2]*National Engineering Laboratory for High Speed Railway Construction, Changsha 410075, China*
[3]*Engineering Technology Research Center for Prefabricated Construction Industrialization of Hunan Province, Changsha 410075, China*

Correspondence should be addressed to Zhipeng Zhai; 514181724@qq.com

Received 29 March 2019; Revised 18 April 2019; Accepted 22 April 2019; Published 30 May 2019

Academic Editor: Eric Lui

This paper develops a novel dry connection utilizing high-strength bolts and introduces the corresponding low-rise precast wall panel structure system. To investigate the seismic performance of the structure system with full bolt connections, monotonic loading tests of the connection joint and cyclic lateral loading tests of three full-scaled precast shear walls are both conducted. Based on the test data, axial and shear mechanical models of the connection are given. Meanwhile, experimental results show that the failure mode of the connection is dominated by anchored rebar ductile rupture, and the precast structure system presents a stable energy dissipation capacity and a good seismic ductility. The numerical model of the precast shear wall is then developed and validated by the cyclic loading test. Also a simplified calculation method to predict the lateral strength of the precast shear wall is proposed. According to the calculation results, the distance between the center of the connection and the edge of the shear wall is suggested to be 150 mm, while the wall thickness is recommended to be 120 mm or 150 mm. Finally, a three-story precast wall panel structure is employed to assess the collapse performance of the proposed precast structure system by using the presented numerical model. The results indicate that the proposed structure system with full bolt connections has high stiffness and high seismic resistance against collapse.

1. Introduction

Precast concrete structure has been widely used because of the distinct advantages of high quality, high industrialization level, fast construction speed, low labor intensity, and green construction [1–8]. Over the last decades, many countries and regions, such as the United States, Japan, China, and Europe, have been increasingly advocating the precast concrete structure system for residential and industrial buildings [3, 4]. Especially, the low-rise precast structures, most of which adopt the precast wall panel structure system [2, 3, 9, 10], have a wide application in building construction [2, 3]. Meanwhile, previous studies have shown that the structure system adopting precast reinforced concrete shear wall as the main lateral resistance component exhibits a good seismic performance [11–13]. At present, many low-rise precast wall panel structure systems have been reported. Xu et al. [1] has conducted quasi-static test to verify the validity of sleeve connection to be used in the precast shear wall. The maximum interstory drift angle of the precast specimen approached 1/56. And the results showed that the precast specimen behaved similarly to the cast-in-situ specimen with respect to failure mode, interstory drift angle, ultimate force, ductility, stiffness degradation, and energy dissipation capacity. Brunesi and Nascimbene [3] proposed a new type of lightly reinforced concrete precast shear wall structure for low-rise residential building, which is connected by using threaded anchors and bolts. The seismic performance and damage pattern of the shear wall were studied by the pseudostatic test, and it showed that there is large residual deformation in the connection joints. Lim et al. [10] presented a type of precast concrete T-wall structural system with C-shaped steel plate connected, and the seismic performance and connection's reliability were verified by the quasi-static test. Gavridou [14] carried out a shaking table test of a full-scale posttensioned concrete wall building, and under strong earthquake excitation, the structural damage was repairable and no prestress loss was found despite the interface grout crushed partially.

The seismic performance of the precast wall panel structure system generally depends on the behavior of connection. The connection type not only affects the manufacture and installation process of precast components but also determines the overall structural performance. Great efforts have been made to investigate the mechanical performance of various connection types of precast wall panel structures, such as types of sleeve [1], emulative [5], hybrid [6], bolted [10], grouted [11, 15], and friction connection [16, 17]. In the previous research, the dry connection presented great advantages for low-rise precast buildings, in terms of quick erection, maintenance, and reuse [18]. Steel plate and bolts are commonly used to create dry connections. Lago et al. [16] and Bora et al. [19] proposed a connection consisting of steel plates, brass plates, and bolts. The well hysteresis behavior and energy dissipation capacity of the connection were demonstrated by quasi-static load tests. Guo et al. [17] developed a friction device composing of two steel angles and one T steel, which were bolted in the connection joint of the column and wall. And low-cyclic load test had shown that the friction device provided good energy dissipation and was controllable and readily replaceable. Bournas et al. [18] carried out the monotonic load test for one type of dry connection, which used bolts and two thick steel plates to connect the longitudinal rebar of the wall joints. The results revealed that this connection has good ductility, and its failure mode is the break of longitudinal rebar. Sun et al. [20] presented a H-shaped horizontal connector welded by a web plate and two flange plates, and two identical wall-connector assembly specimens were tested under monotonic loading and cyclic loading. The results showed that the performance of the shear walls was satisfactory in terms of ensuring the shear wall strength and ductility.

Since 21st century, the world has entered a seismic-prone period. More challenges are raised for the development of precast buildings. Especially the countries like China where high seismic intensity areas are widely distributed and facing the problem of reconstruction in disaster areas and urbanization construction. In such circumstances, the developmental potential of the low-rise shear wall structure is gradually highlighted. Dry connection has been proven to be effective for the low-rise precast wall panel structure system in previous studies. However, more fast development and effective assembly connection are significant for reconstruction of disaster areas. In this paper, a new type of dry connection, which is more convenient for installation and composed of steel plates and high-strength bolts, is developed. Also the corresponding low-rise precast wall panel structure system with full bolt connections is introduced. The static loading test of the connection is conducted to investigate the joint performance. Then three full-scaled specimen of the precast concrete wall with bolt connections is cyclically tested. In order to describe the nonlinear behavior of the precast shear wall and evaluate the overall performance of the precast low-rise building, a finite element model (FEM) modified by the test data is developed. And a simplified method to calculate the lateral strength of the precast shear wall is derived. Considering the failure of connection is usually the main cause of collapse [21], the adjusted collapse margin ratio of a three-story precast wall panel structure is assessed based on pushover analysis.

2. Description of the Novel Dry Connection

The proposed novel dry connection in this paper consists of anchored steel plate and high-strength bolt. Figure 1 depicts the details of the connection. The steel plate adopts the Q345 steel with the nominal yield strength of 345 MPa and is anchored by using the HRB400 rebar with a nominal yield strength of 400 MPa. Grade 10.9 high-strength bolts with the nominal yield strength of 900 MPa are used to install the walls. Figure 2 describes the details of the vertical connection joint, and the horizontal joint is similar. As the reinforcement in the precast wall panels are discontinuous, all precast components can be erected conveniently. To ensure the performance of the connection, the anchored steel plate should be carefully designed to avoid the early failure, such as pullout of the anchored steel plate and bending of the steel plate. Current design codes, such as GB 50011-2010 [22] and ASCE [23], can be adopted to design the dry connection. The basic configuration of the low-rise precast wall panel structure system is displayed in Figure 3. Thickness of the walls is 150 mm, and all the precast wall panels are connected by the dry connections. The concrete walls work as a tube to transfer the gravity load and lateral load. This precast structure system has a rapid assembly advantage, and the main structure can be constructed at site within one day. It has been employed in practical engineering [24].

3. Experiment of the Connection Joint

To investigate the static behavior and obtain the axial and shear force-displacement models of the bolt connection joint, monotonic tensile and shear test are performed in this section. The axial and shear force-displacement models are used for establishing numerical model of precast shear walls in Section 5. Therefore, the designing parameters of the specimens in the monotonic test are the same as the precast wall. In order to avoid randomness and unreliability, three same specimens are constructed for tensile test, as well as the shear test.

3.1. Tensile Test

3.1.1. Test Specimens and Setup. The specimens for the axial tensile test consist of connection described in Section 2 and C30 concrete (nominal compressive strength f_{cu} equals to 30 MPa) block. Its dimensions are 1200 mm high, 400 mm

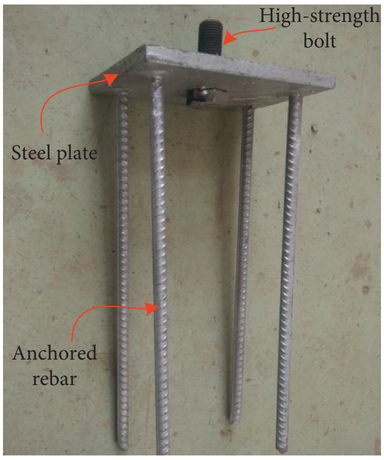

Figure 1: Details of a typical embedded dry connection.

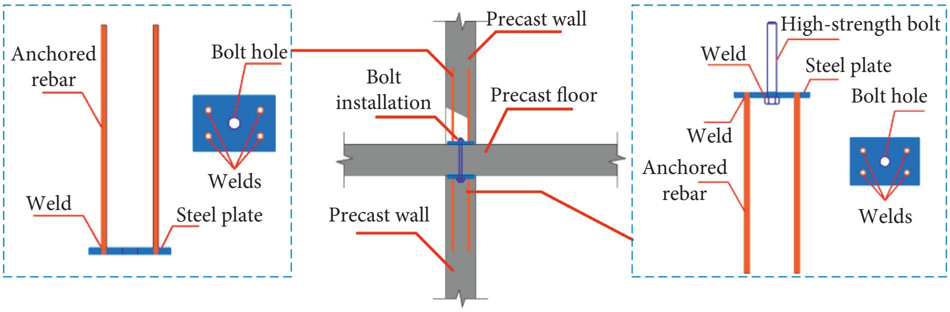

Figure 2: Details of the connection joint of the precast components.

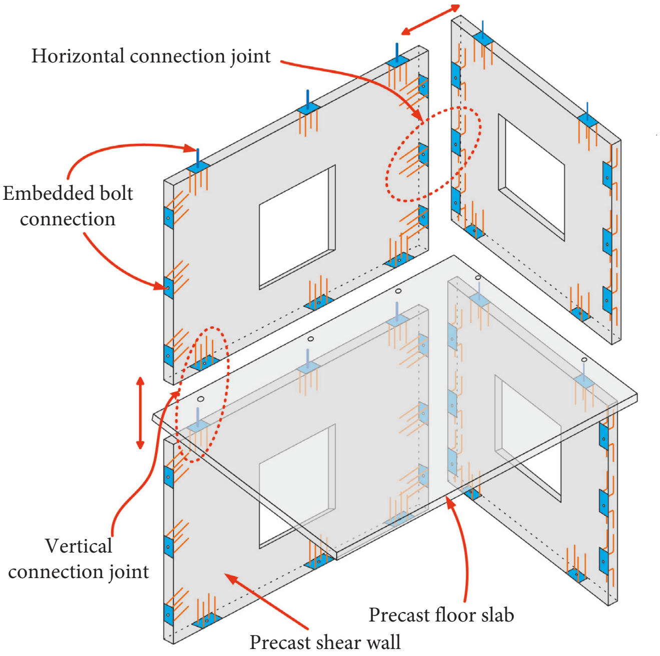

Figure 3: Low-rise precast structure system with full bolt connections.

wide, and 150 mm thick, as shown in Figure 4(a), where Φ represents the HRB400 steel bar. Figure 4(b) depicts the details of embedded connection. The steel plate with dimensions of 180 mm (height) × 130 mm (width) × 14 mm (thickness) is anchored by four steel bars. And the length of the steel bars is 420 mm. Diameters of the steel bars and grade 10.9 high-strength bolts are 12 mm and 22 mm, respectively.

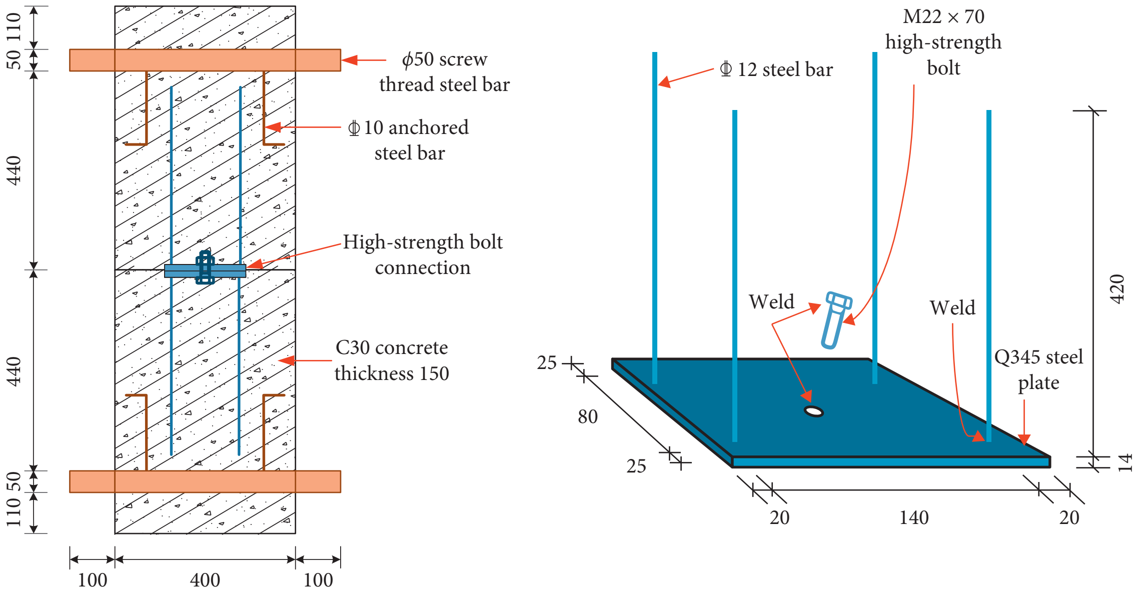

(a) (b)

Figure 4: Configuration of the testing connection joint (unit: mm): (a) dimensions of the specimen and (b) dimensions of the embedded connection.

Three same specimens marked as T1, T2, and T3 were tested by monotonic axial loading. Before test loading, the 550 N·m torque was applied to fasten the high-strength bolt according to the Code for design of steel structures [25], which can be calculated by the following expression:

$$T = k \cdot P \cdot d, \tag{1}$$

where T is the torque; P is the pretightening force, which equals to 190 kN based on the code [25]; d is the diameter of the high-strength bolt, which is 22 mm; k is the torque coefficient, which adopts 0.13 [25]. The monotonic loading process adopted force and displacement double control. During the force control stage, each load step was increased by 10 kN until the load reached 70 kN. Then each step was increased by 5 kN till the specimens cracked. After that, displacement loading was implemented till the specimen fails. During the test, one displacement sensor (DS) was used to monitor the connection behavior, as shown in Figure 5. According to the Chinese code, specification of testing methods for earthquake-resistant building [26], when the peak load of a loading cycle dropped to less than 85% of the maximum load, the specimen is defined to be destroyed and the test is terminated.

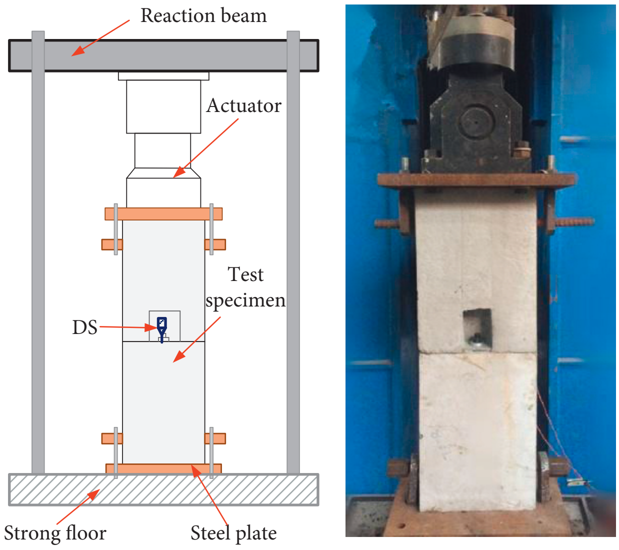

(a) (b)

Figure 5: The axial tensile test setup: (a) test setup of the specimens and (b) test setup.

3.1.2. Test Results. Damage of the specimens was observed during the test. Before the axial loading, transverse fine crack was induced by the applied torque. It propagated slightly at the end of the test. Figure 6 shows the finial failure mode of each specimen. In general, the three specimens failed with the similar mode. The failure process of the specimen can be described as (a) before the load was lower than 80 kN, no visible damage was observed, and the specimens were elastic; (b) while the load increased to 80 kN, the anchored rebar began to slip, it then caused the concrete to crack at the load of 120 kN, and the steel plate started to yield and bend; and (c) when the displacement control load started, concrete spalled gradually and the steel plate bent seriously. Subsequently, the connection failure that was characterized by the rupture of the anchored rebar in the weld point occurred when the displacement approached to 22 mm. In summary, the failure mode in the connection joint can be described in the following sequence: anchored rebar slipped, concrete cracked, steel plate bent, and anchored rebar ruptured. It

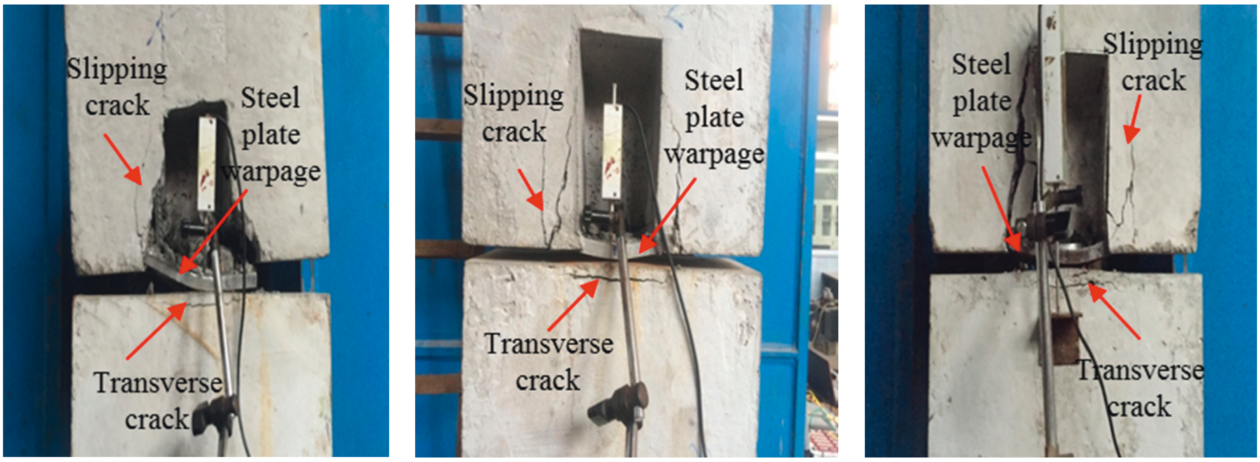

(a) (b) (c)

Figure 6: Failure modes of the specimens during the tensile test: (a) T1, (b) T2, and (c) T3.

should be noted that the failure, including steel plate bending and rebar rupture, exhibited good ductile behavior.

Figure 7 gives the axial load-displacement curve of the three specimens. The specimens have large initial stiffness. The stiffness decreases obviously at the load of about 80 kN and 120 kN due to the anchored rebar slipping and steel plate bending. For establishing a numerical model in the later section, the axial mechanical model representing the axial force-displacement relationship is obtained by adopting the mean value of load and displacement at the critical loading points, such as cracking and yielding points. Because the lateral load drops rapidly as a result of connection failure at the displacement of about 22 mm, a sudden drop is defined for the axial mechanical model to reflect the connection failure. Moreover, the load and displacement values for different loading phase of the three specimens are provided in Table 1.

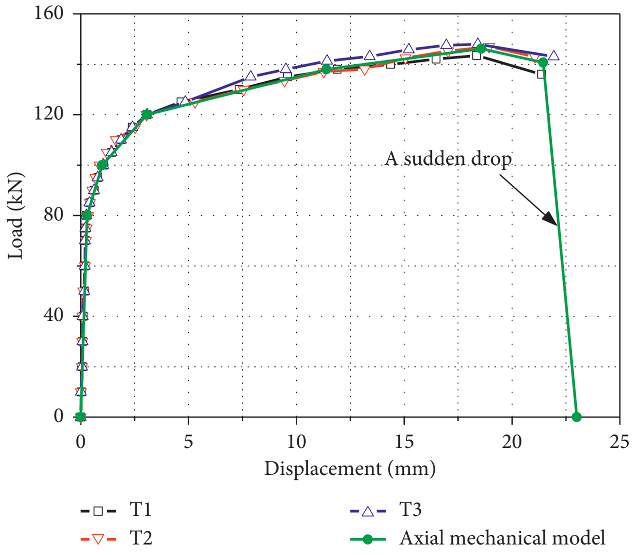

Figure 7: Axial load versus displacement curve.

3.2. Shear Test. Three identical specimens, marked as S1, S2, and S3, were constructed to be tested in the monotonic shear loading. The design parameters were the same as the tensile test specimens. The monotonic shear loading was applied by using a hydraulic jack. Two displacement sensors (DSs) were used, and the relative location of the two DSs is shown in Figure 8. And their relative displacement would be measured as the shear displacement of the connection joint.

Figure 9 compares the shear failure modes of the three test specimens. It can be observed that the failure mode of each specimen was similar. The failure process can be depicted as follows: (a) at the beginning of the test, the applied loading was smaller than the friction. The displacement was proportional to the shear load, and the specimens were elastic. (b) With the load near 80 kN, the connecting bolt began to slip as the shear force was larger than the friction. Then, the sliding stopped around the load of 110 kN due to the contact of the screw rod and steel plate. (c) At the load of 170 kN, concrete began to crack and spall, which was induced by the bond-slip effect of the anchored rebar. When the load neared 220 kN, the anchored rebar of S1 and S3 fractured, while S2 lost bearing capacity due to the serious bending of the anchored rebar. In summary, sequence of the shear failure of the connection joint can be listed as follows: the bolt slipped, concrete cracked, and anchored rebar ruptured. Figure 10 shows the shear load-displacement curves of the three specimens. The dramatic degradation of the shear stiffness at load about 80 kN is caused by the bolt slipping. And contact of the screw rod and steel plate leads to the significant stiffness hardening at a load of about 110 kN. For establishing the numerical model in the later section, the shear mechanical model representing the axial force-displacement relationship is also obtained by the test data. In addition, the load and displacement values for different loading phase are provided in Table 2.

4. Experiment of Precast Shear Wall

4.1. Wall Specimen. Three full-scaled precast shear wall specimens with different axial compressive ratios are

Table 1: Results of the tensile test.

Specimen	Slipping load and displacement		Cracking load and displacement		Peak load and displacement		Ultimate load and displacement	
	V_s (kN)	Δ_s (mm)	V_{cr} (kN)	Δ_{cr} (mm)	V_p (kN)	Δ_p (mm)	V_u (kN)	Δ_u (mm)
T1	80	0.276	120	3.076	143	18.359	136	21.369
T2	80	0.340	120	3.054	147	18.935	143	21.057
T3	80	0.266	120	3.076	148	18.415	143	21.938
Mean value	80	0.294	120	3.069	146	18.569	141	21.455

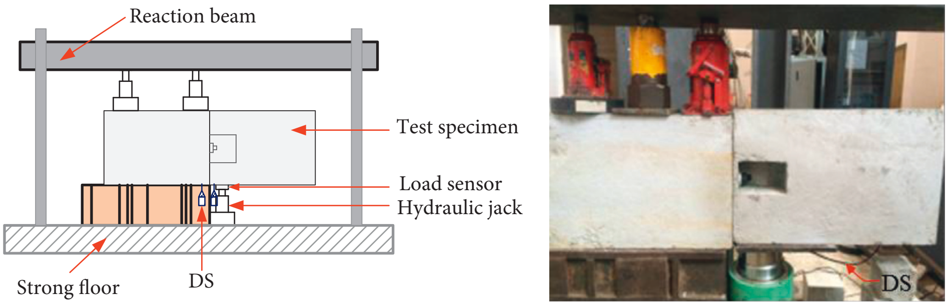

(a) (b)

Figure 8: The shear test setup.

(a) (b) (c)

Figure 9: Failure mode of the specimens during the shear test: (a) S1, (b) S2, and (c) S3.

constructed to investigate the seismic performance of the proposed wall system. The three specimens are named SW1, SW2, and SW3 here, corresponding to the axial compressive ratios of 0, 0.1, and 0.2, respectively. Designing parameters of these specimens are the same. The wall height is 3000 mm, the width is 1550 mm, and the thickness is 150 mm. Configuration and reinforcement details of the test specimens are drawn in Figure 11. The wall longitudinal and transverse reinforcement adopts the HRB400 steel bar with the diameter of 6 mm, and the C30 concrete is used. As shown in Figure 11, the longitudinal reinforcement is discontinuous, and the precast shear wall is connected to the rigid foundation beam by two dry connections. Dimensions of the foundation beam are 2500 mm × 800 mm × 600 mm. Design parameters and construction details of the connections are the same as static tests above. The installing holes are filled by using C35 fine aggregate concrete with 35 MPa nominal compressive strength. The interface between the wall and foundation beam is filled by ceramic tile adhesive. The distance between center of the connection and edge of the shear wall, marking as *d*, is 100 mm.

4.2. Test Setup and Loading History. The details of the test setup are shown in Figure 12. The specimens are fixed to the strong floor through six anchored bolts. Reversed cyclic lateral loads are applied to the specimen by using a 1000 kN hydraulic actuator that is mounted to a reaction wall. The distance from the center of the actuator to the bottom of the shear wall is 2750 mm. Thus, the shear-span ratio for the bottom section of the wall can be calculated as 1.77. A steel girder is installed on the top of the shear wall to distribute the vertical load, while the vertical load is simulated by using a hydraulic jack placed on the steel girder. The reaction force of the hydraulic jack is transferred to the strong floor by using the four thread steel bars mounted around the shear wall. Four displacement sensors are instrumented in the lateral direction to monitor the shear wall behavior. The relative displacement between DS1 and DS4 is measured as the shear wall displacement.

First step of the test is to impose the axial load. For these specimens, the applied axial loads are 0 kN, 332 kN, and 664 kN, corresponding to the precast walls SW1, SW2, and

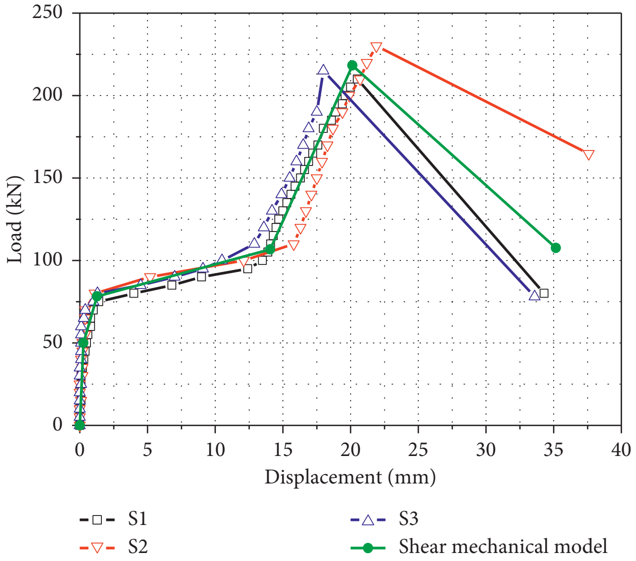

Figure 10: Shear load versus displacement curve.

Table 2: Results of the shear test.

Specimen	Slipping load and displacement		Cracking load and displacement		Peak load and displacement		Ultimate load and displacement	
	V_s (kN)	Δ_s (mm)	V_{cr} (kN)	Δ_{cr} (mm)	V_p (kN)	Δ_p (mm)	V_u (kN)	Δ_u (mm)
S1	75	1.4	170	17.6	210	20.5	80	34.3
S2	80	1.1	170	18.3	230	21.9	165	27.6
S3	80	1.3	170	16.5	215	18.0	78	33.6
Mean value	78.3	1.3	170	17.5	218	20.1	107.7	35.17

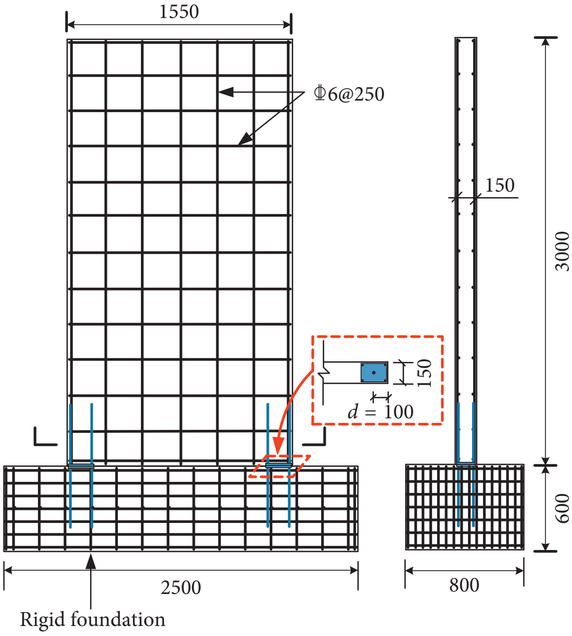

Figure 11: Configuration and reinforcement details of the precast shear walls (unit: mm).

SW3, respectively. The cyclic lateral loads applied by using the actuator are in accordance with the test loading history, as shown in Figure 13. The force and displacement double control loading are employed during the test. In the process of the force control stage, each load level is maintained for one cycle till the specimen yield. Then the displacement control is implemented, and each load level increases by one yield displacement. Meanwhile, each level is implemented for two cycles till to the specimen failure. During the cyclic lateral test, there are 6 load levels, 10 load levels, and 10 load levels for SW1, SW2, and SW3, respectively. When the peak load of a loading cycle dropped to less than 85% of the maximum load, the specimen is defined to be destroyed, and the test is terminated [26].

4.3. Test Results

4.3.1. Failure Mode. An identical failure mode for the specimens was observed during the test. All the specimens failed as the result of connection rupturing and presented similar damage evolution. Due to failure behavior of the three specimens are similar, the damage evolution of typical wall SW2 is described here in detail. Figure 14 depicts the damage pattern of the test specimen SW2. The initial tension crack on the filled interface between the wall and foundation occurred at the load of 100 kN, as shown in Figure 14(a). When the load approached to 170 kN, which corresponds to the displacement of 11.27 mm, vertical compression crack in the wall corner appeared, as shown in Figure 14(b). As the load increased continuously, concrete in the compression zone spalled and crushed gradually, and anchored steel bars

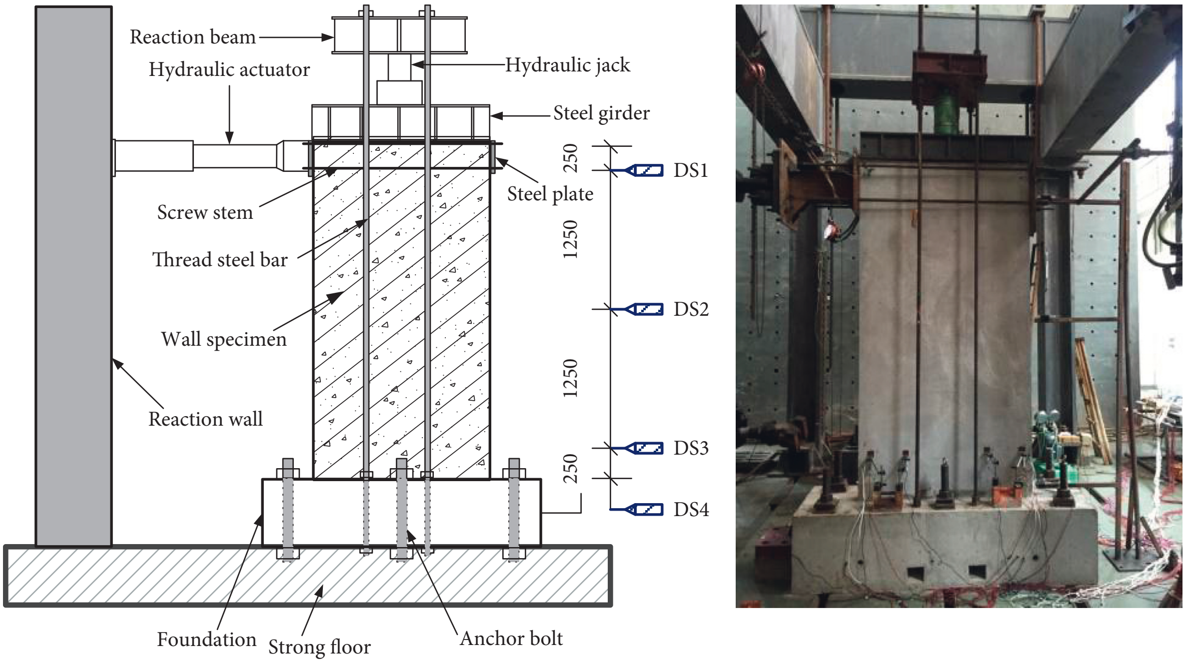

(a)

(b)

FIGURE 12: The details of test setup (unit: mm): (a) test setup of the specimen and (b) test picture.

of the connection were bent by compressive stress. Meanwhile, bending deformation of the steel plate in the tension zone occurred. After reaching the ultimate load, corresponding to the displacement of 26.45 mm in the positive direction and 29.28 mm in the negative direction, the lateral load degraded dramatically due to the failure of anchored steel bar rupturing. During the cyclic loading test, no shear cracks on the wall were observed, and damages were concentrated on the connection joints. The failure mode of the test specimen is shown in Figure 14(c). In summary, the failure mode of the specimens is presented as the concrete crushing and connection rupturing, which is mainly induced by the flexural tensile stress.

4.3.2. Hysteretic Behavior and Energy Dissipation. The hysteretic and backbone curves of the specimens are drawn in Figure 15. At the initial loading stages, the specimen performed elastic basically. At the displacement control loading stages, the stiffness decreased obviously and the energy dissipation increased gradually as a result of nonlinear plastic behavior and damage of the specimen. It can be observed that axial compressive ratio has significant influence on the energy dissipation and bearing capacity. Increasing the axial compressive ratio, the lateral strength and area of hysteresis loop increase significantly. Pinching effect can be observed in the plastic stage, especially for SW2 and SW3, indicating wall displacement was influenced by shear deformation or wall sliding. Moreover, it can be observed that the test specimen had a long yielding platform.

In the loading cycles, residual displacement may generate. The residual displacement and maximum displacement in each load level are compared in Figure 16. The residual displacement for each loading cycle is defined as the relative displacement to the wall initial position after unloading. It can be found that residual and maximum displacement increase gradually with the load level, and residual displacement is positively correlated with the maximum displacement of the cycle. Residual displacement of the wall SW1 is obviously larger than those of the walls SW2 and SW3, demonstrating the damage of SW1 develops faster. For SW2 and SW3, the residual displacements are relatively small due to the restriction of axial compressive force. At the early loading stage, residual displacement is very small, with 0.03 mm and 0.07 mm in the negative and positive directions, respectively, for SW2. And they are 0.01 mm and 0.09 mm for SW3. Then they increase to 2.68 mm and 6.22 mm, respectively, in the last load level for SW2 and increase to 0.65 mm and 4.54 mm for SW3. Residual displacement ratios that are defined as the ratio of residual displacement to maximum displacement are 0.15 and 0.21 for SW2 and SW3, respectively, in the finial loading cycle. These illustrate that overall residual displacements of the walls SW2 and SW3 are small and also indicate that sliding friction effect on the connecting interface is slight, otherwise the large residual displacements will be caused due to the friction sliding.

Two important indexes, cumulative dissipated energy and equivalent viscous damping ratio, are adopted to assess the energy dissipation capacity of the test specimen. According to the area of the hysteretic loop in each loading cycle, the energy dissipation of the specimens can be calculated, as shown in Figure 17. The equivalent viscous damping ratio is expressed as [27]

$$\xi_{\mathrm{eq}} = \frac{E_{\mathrm{D}}}{2\pi E_{\mathrm{S0}}}, \tag{2}$$

where E_{D} is the dissipated energy in one hysteresis loop and E_{S0} is the strain energy of an equivalent linear elastic

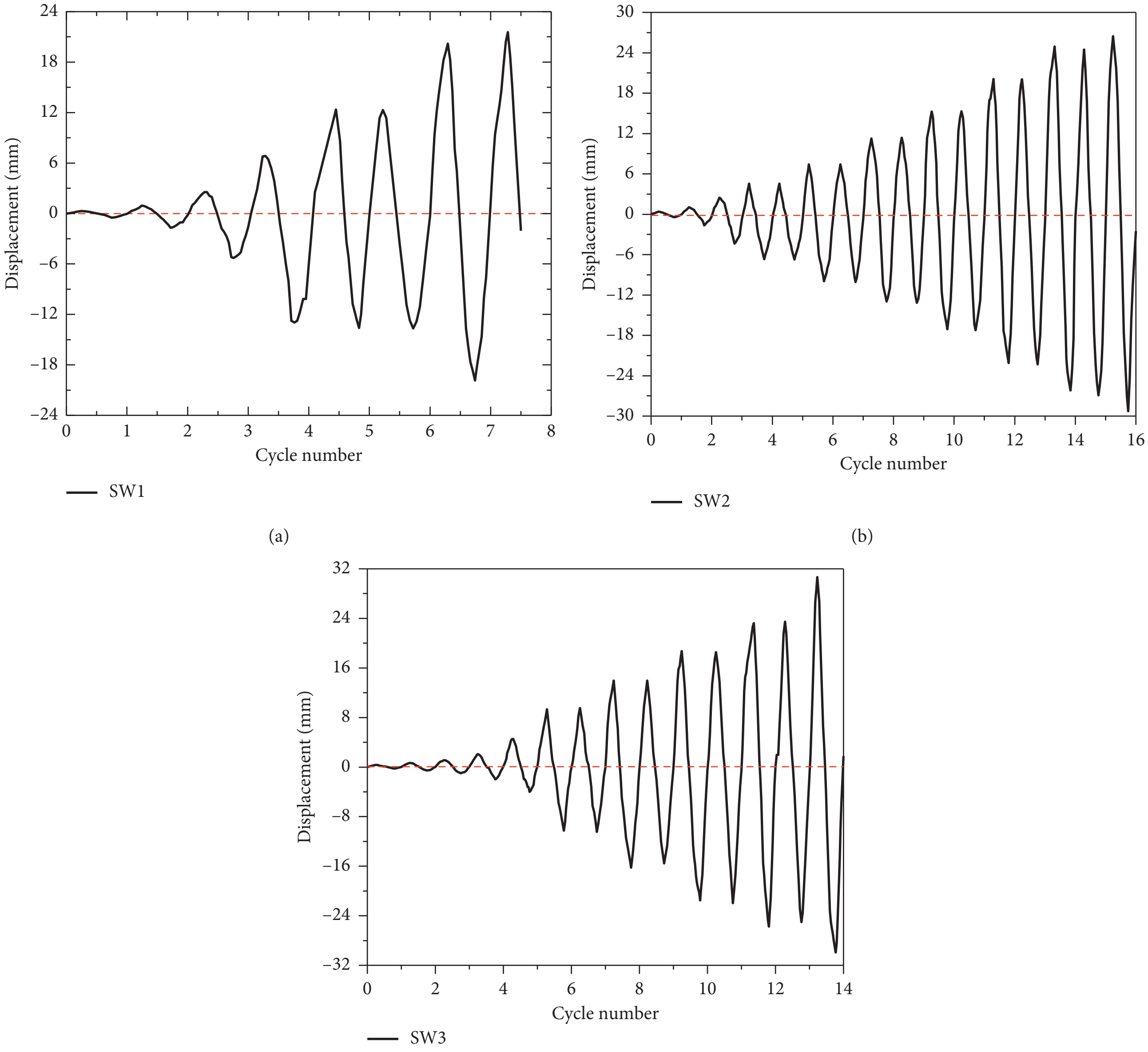

(a)

(b)

(c)

Figure 13: The test loading history.

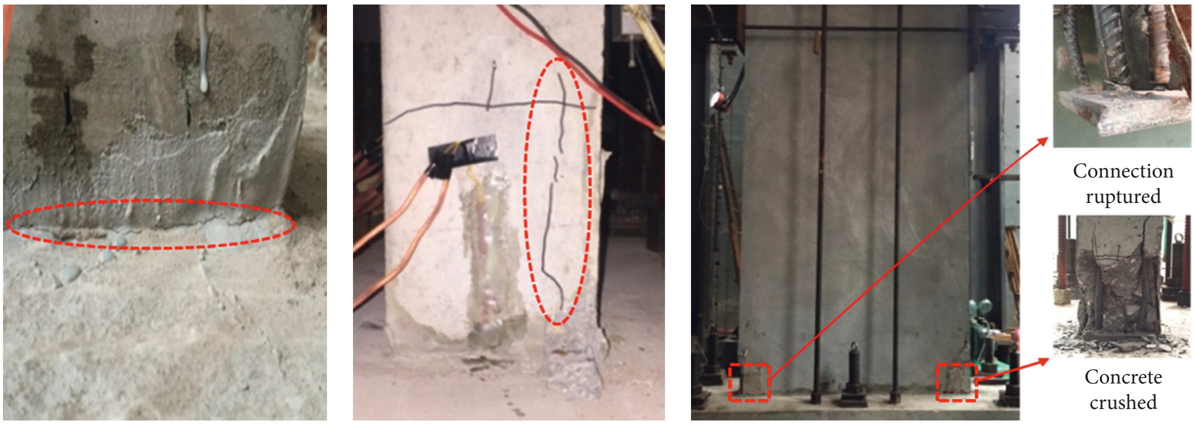

(a)

(b)

(c)

Figure 14: Observed damages of the specimen during the test: (a) tension crack of the filled interface, (b) compressive crack of the concrete, and (c) the failure mode.

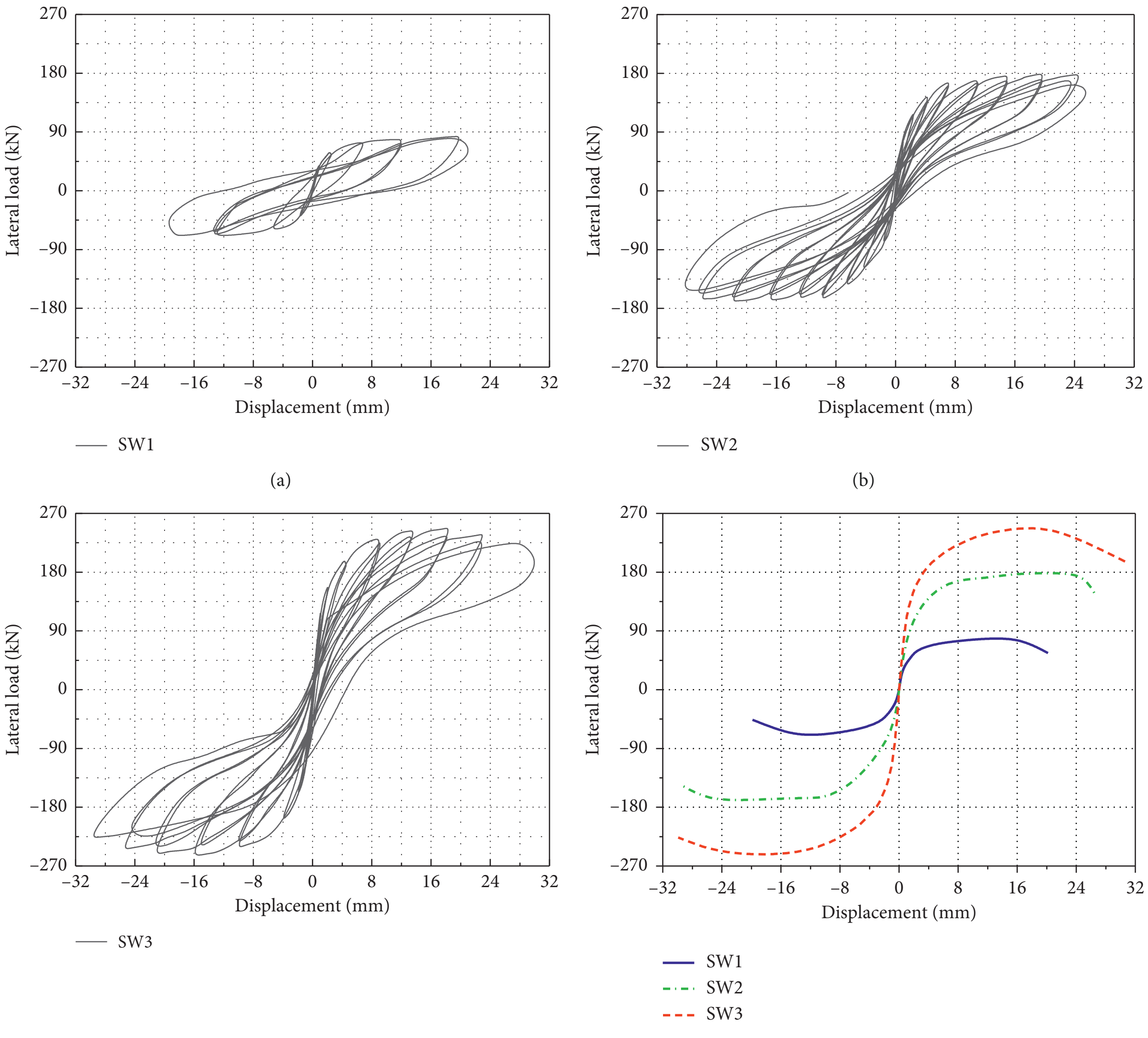

(a)

(b)

(c)

(d)

Figure 15: Hysteretic curves and backbone curves of the test specimens: (a) SW1, (b) SW2, (c) SW3, and (d) backbone curves.

system at maximum displacement. The equivalent viscous damping ratio of the specimen is shown in Figure 18. Because the positive and negative displacements in a given cycle are not identical, the average value of them is adopted to represent the horizontal ordinate in Figures 17 and 18. As observed from the figure, energy dissipation and equivalent damping ratio increase obviously with the increasing load level. The equivalent damping ratio increases from 0.056 to 0.195 for SW1, from 0.047 to 0.142 for SW2, and from 0.073 to 0.125 for SW3. Because the wall SW1 without axial compressive force applied has a smaller bearing capacity and faster damage evolution, it presents a much smaller cumulative energy dissipation and a larger damping ratio. With the increment of axial compressive ratio, the dissipative energy of the wall increase obviously. In general, the walls SW2 and SW3 exhibit a stable energy dissipation capacity.

4.3.3. Ductility and Damage Factor. During the cyclic test, no obvious yielding of longitudinal reinforcements of the wall specimen was observed. Therefore, the yielding point is defined by the principle shown in Figure 19. The ductility is a significant factor to evaluate the seismic performance of structure and component. The ductility factor μ is defined as the ratio of the ultimate displacement Δ_u to the yielding displacement Δ_y. Through calculation, the final results are listed in Table 3. Although the ductility factor has an obvious difference in the negative direction and positive direction, the average ductility factors for walls SW1, SW2, and SW3 are 4.97, 5.03, and 6.09, respectively. That is, the test specimen possessed a good seismic ductility. The stiffness degradation usually determines the damages of structure and component. Hence, a damage factor is also defined in this paper, which is represented by the change of secant stiffness. It can be expressed as [28]

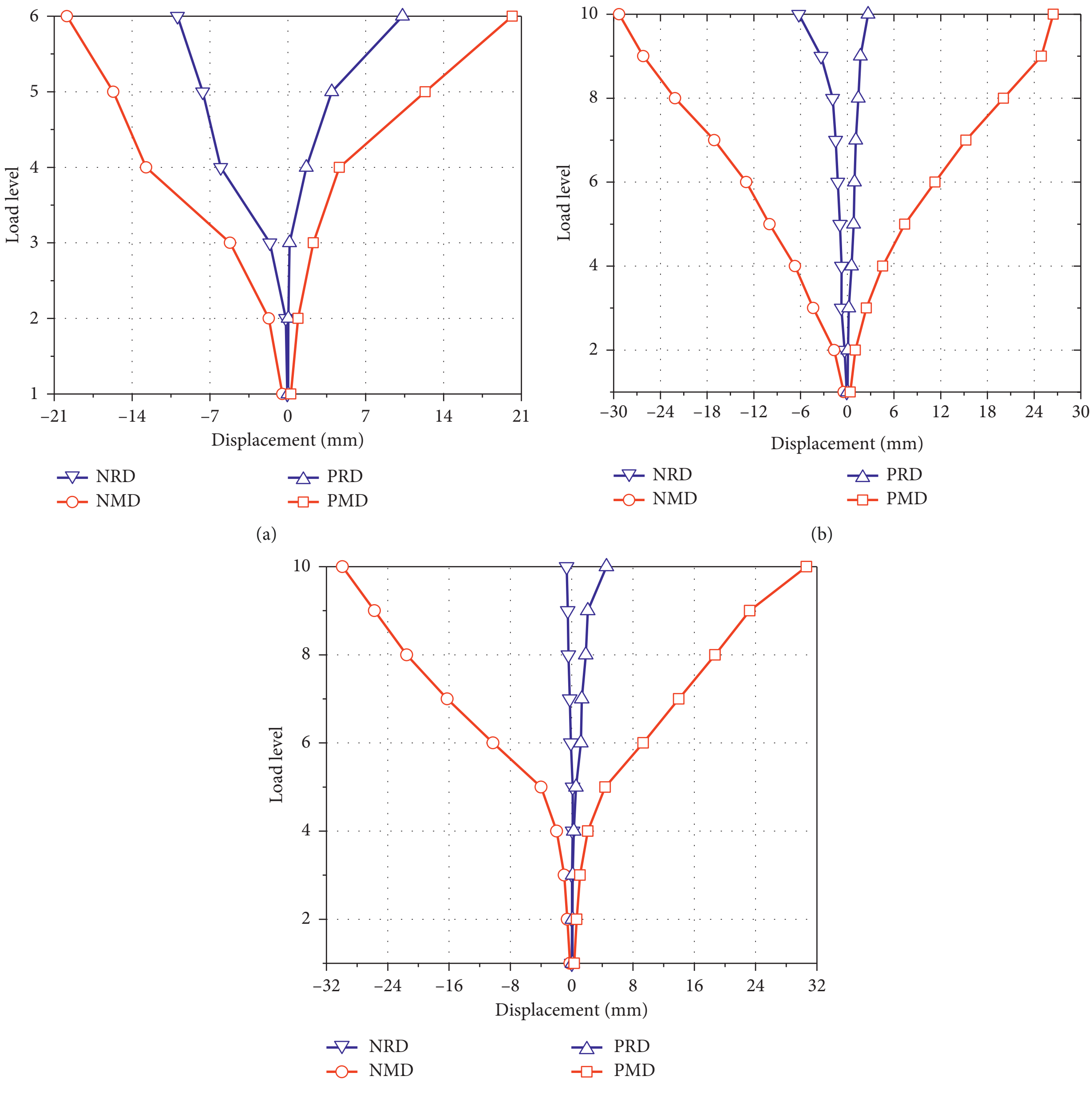

(a)

(b)

(c)

Figure 16: Comparison of residual and maximum displacements (NRD: negative residual displacement; NMD: negative maximum displacement; PRD: positive residual displacement; PMD: positive maximum displacement): (a) SW1, (b) SW2, and (c) SW3.

$$D_i = 1 - \frac{K_i}{K_0}, \tag{3}$$

where D_i is the damage factor of ith load level, K_i is the secant stiffness of ith load level, and K_0 is the initial secant stiffness. It is clear that the lager damage factor indicates more serious damage. The damage factors of the test specimens are depicted in Figure 20. At the early loading stage, the damage factors in the negative direction are larger than those in the positive direction. However, there is only a little discrepancy after the specimen yielding. At the peak point, the damage factors range from 0.89 to 0.92. At the ultimate point, the damage factors range from 0.94 to 0.96. The stable variation of damage factors after the specimen yielding is the result of the identical failure mode of the specimens. To ensure seismic safety, a conservative value of damage factor, 0.9, is suggested for the performance state of collapse prevention.

5. Numerical Analysis

5.1. Modeling. An effective approach to numerically simulate shear wall component is proposed to adopt the multilayer shell element [29]. To predict the nonlinear behavior, a finite element model (FEM) of the tested precast shear wall is established, as shown in Figure 21. The software ETABS is adopted. The precast shear wall is modeled by using the multilayer shell element, which contains one concrete layer and four steel bar layers. The stress-strain relationship of

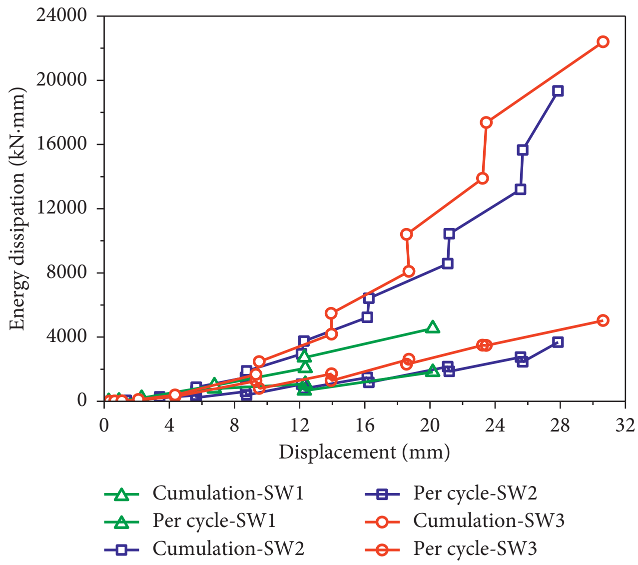

FIGURE 17: Energy dissipation of the specimens.

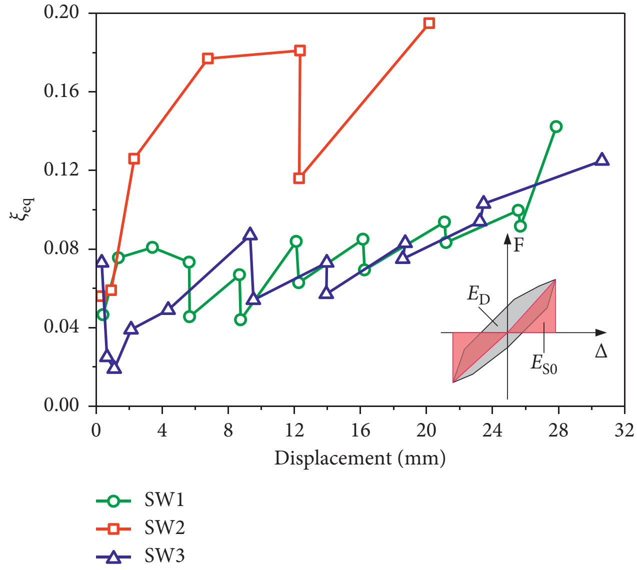

FIGURE 18: Equivalent viscous damping ratio of the specimens.

concrete and steel bar is given in Figure 22, in which the concrete strength adopts $0.88f_{cu}$ according to the Chinese code [30], and steel strength adopts measured yield strength 400 MPa and ultimate strength 570 MPa. In order to simulate the dry connection joint, nonlinear zero-length element is utilized. Axial and shear mechanical models of the connections have already been obtained by monotonic loading tests, as drawn in Figures 7 and 10. Interface contact effect between foundation and wall is also a vital factor needed to be considered. The friction isolator element, employing a high vertical stiffness and friction coefficient of 0.6, is implemented to simulate the contact effect.

Here, the specimen SW2 is numerically simulated to verify the modeling approach. Figure 23 shows the stress distribution of FEM in the failure state, and it is in accordance with the damage state observed at the end of the test (Figure 14). The numerical analysis indicates that the wall is destroyed as a result of connection rupturing, the same failure mode as the test specimen. The backbone curve and damage factor of FEM and experiment are compared in Figure 24, which shows that simulation results match well with the experimental results. The methodology of the proposed FEM is validated.

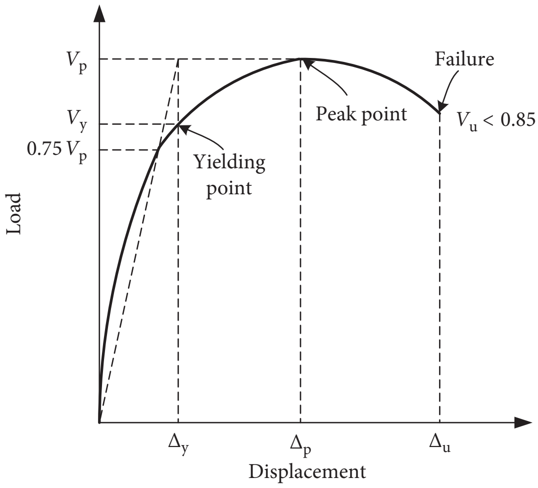

FIGURE 19: The definition of the yielding point.

5.2. FEM Modification. The axial and shear behaviors of the connections are considered uncoupled in Section 5.1, making the connections more ductile. Hence, the FEM failed to capture the breakdown performance, as shown in Figure 24(a). In order to give more accurate simulation, axial load-displacement behavior of the connections is modified until a satisfactory match was achieved between the FEM and the experimental results. Figure 25 compares the backbone curves and damage factors of modified FEMs (MFEMs) and test specimens, while the critical deformation and load value are listed in Table 4. Although there are some differences with regard to the backbone curves between the MFEM and the tests, especially for SW3, the initial stiffness, peak load, and ultimate displacement of MFEM match well with those of the experimental results. And the MFEMs can capture the breakdown performance. Damage factors of MFEMs are slightly greater than that of the experiment, but they are still in good accordance with experiment on the whole, illustrating that the damage evolution can be simulated by the MFEMs. In general, the simulation results are in good agreement with the experimental results. The differences between the MFEMs and the test maybe mainly caused by the following reasons: (a) coupling effect of axial and shear behaviors of the connections is not fully considered in the MFEMs; (b) interfacial friction coefficient, adopted as 0.6, may have difference from the actual component; (c) the connections are simulated by using the macroscopic element (link element) based on the static test result, which do not consider the bonding slip behavior between the connection and the wall fully.

Table 3: Data of the cyclic lateral test.

Specimen	Direction	V_{cr} (kN)	Δ_{cr} (mm)	V_y (kN)	Δ_y (mm)	V_p (kN)	Δ_p (mm)	V_u (kN)	Δ_u (mm)	μ	μ'
SW1	Positive	40	0.93	62.96	2.99	78.9	12.35	67.01	18.33	6.13	4.97
	Negative	−40	−1.7	−56.93	−4.43	−70	−12.74	−59.5	−16.84	3.80	
SW2	Positive	100	1.54	149.63	4.62	178.6	20.08	151.81	26.25	5.68	5.03
	Negative	−90	−1.95	−146.01	−6.69	−169.8	−22.12	−147.5	−29.28	4.38	
SW3	Positive	160	2.11	203.24	4.86	249.8	18.72	212.33	27.75	5.71	6.09
	Negative	−160	−1.96	−204.32	−4.63	−252.9	−16.24	−226.3	−29.91	6.46	

V_{cr} and Δ_{cr} represent the cracking load and displacement; V_y and Δ_y represent the yielding load and displacement; V_p and Δ_p represent the peak load and displacement; V_u and Δ_u represent the ultimate load and displacement; μ represents the ductility factor; μ' represents the average ductility factor.

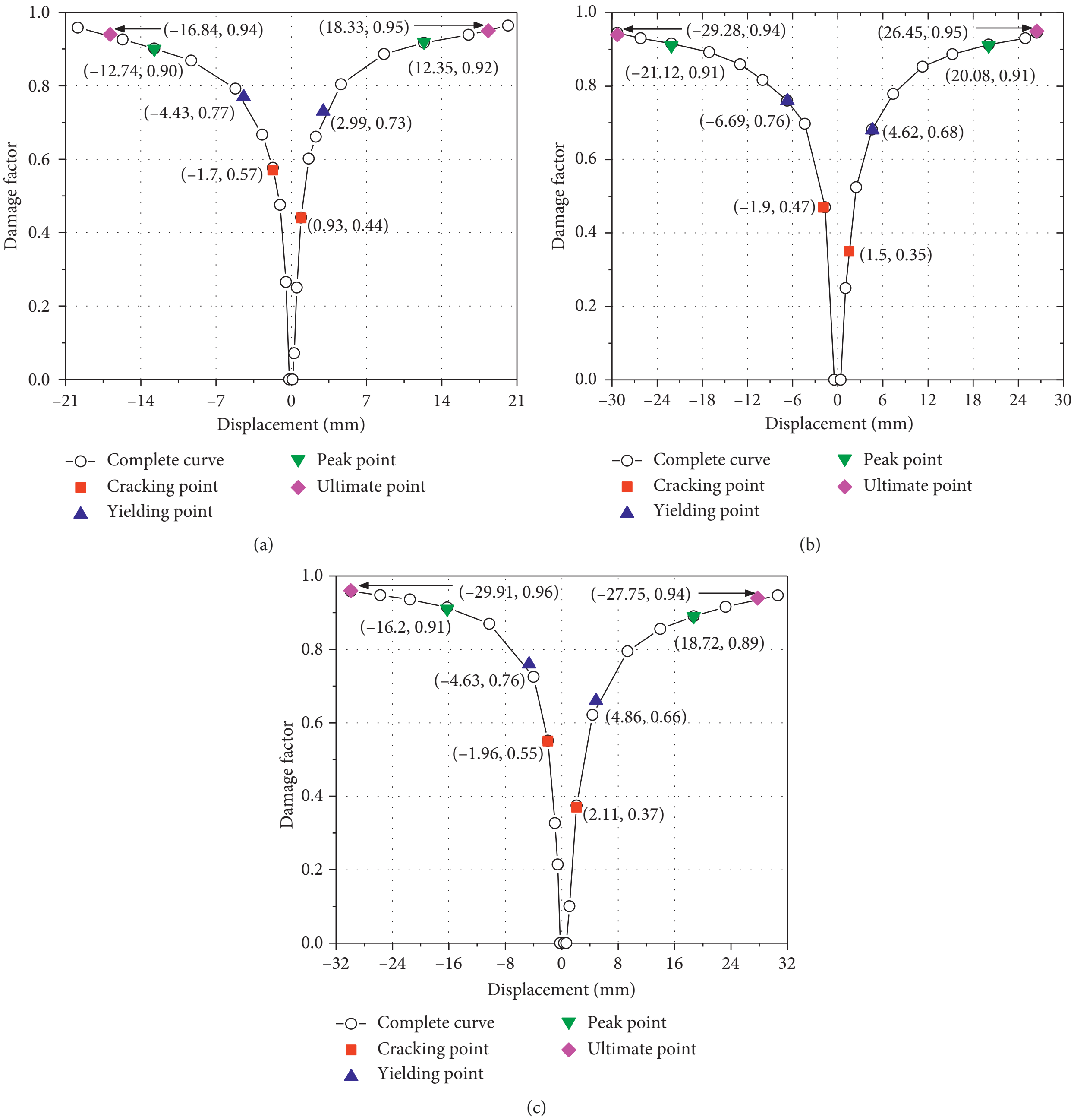

(a) (b) (c)

Figure 20: The damage factors of the test specimens: (a) SW1, (b) SW2, and (c) SW3.

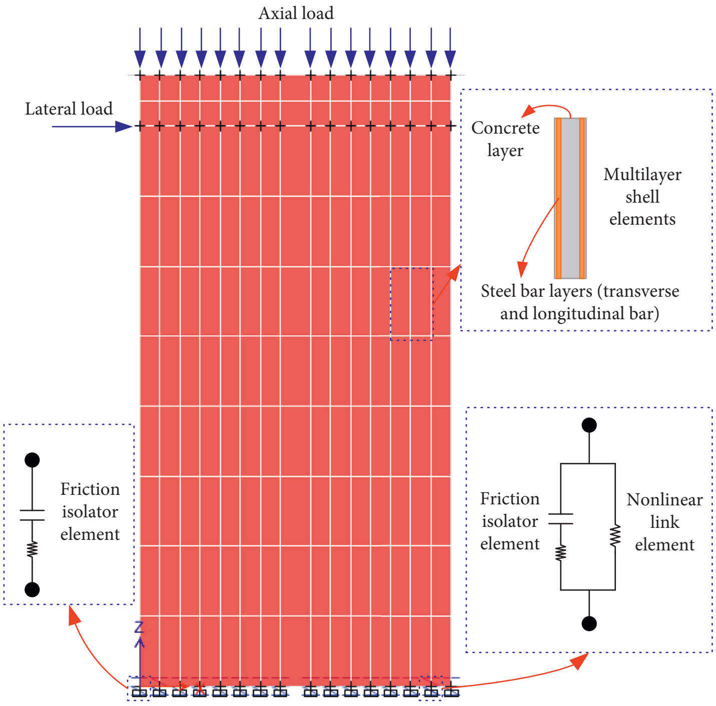

Figure 21: Modeling based on ETABS.

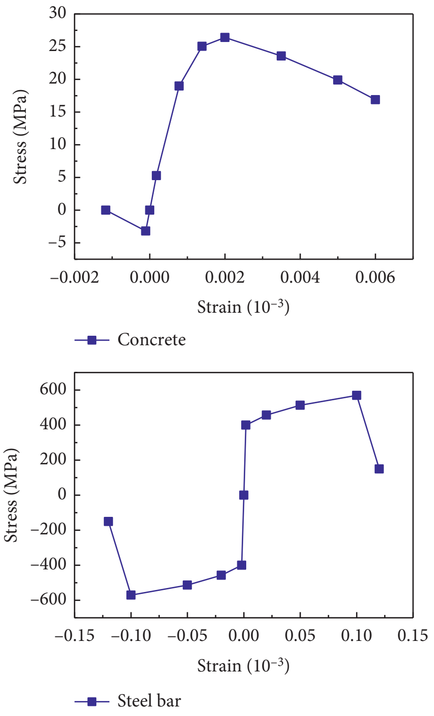

Figure 22: Constitutive models of concrete and steel bar.

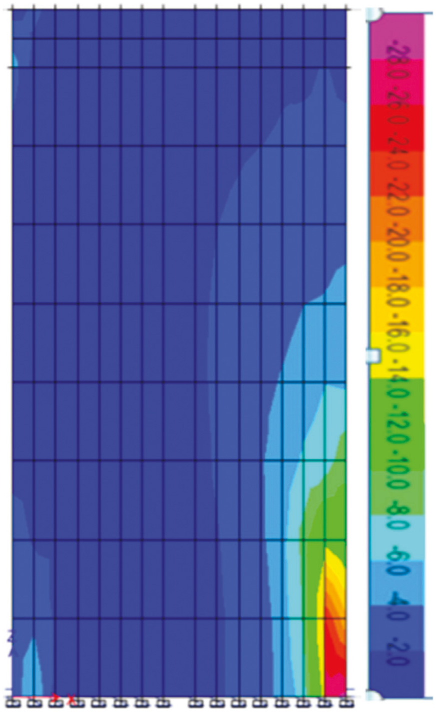

Figure 23: Distribution of concrete stress of SW2 FEM.

Figure 26 plots the internal force of the dry connection in MFEM-SW2, shear force of which is larger than MFEM-SW1 and -SW3. As the displacement reached 22.79 mm, the connection is ruptured by axial tensile force. Then the lateral load drops rapidly due to the failure of the connection. The shear force 79.46 kN is slightly larger than tangential slipping force 78.3 kN (Table 2), demonstrating that the wall slid slightly. The analysis on the above indicates that the MFEMs can predict the nonlinear responses of the precast wall panels, and it can be used to study the overall mechanical performance of the precast low-rise structure with bolt connection.

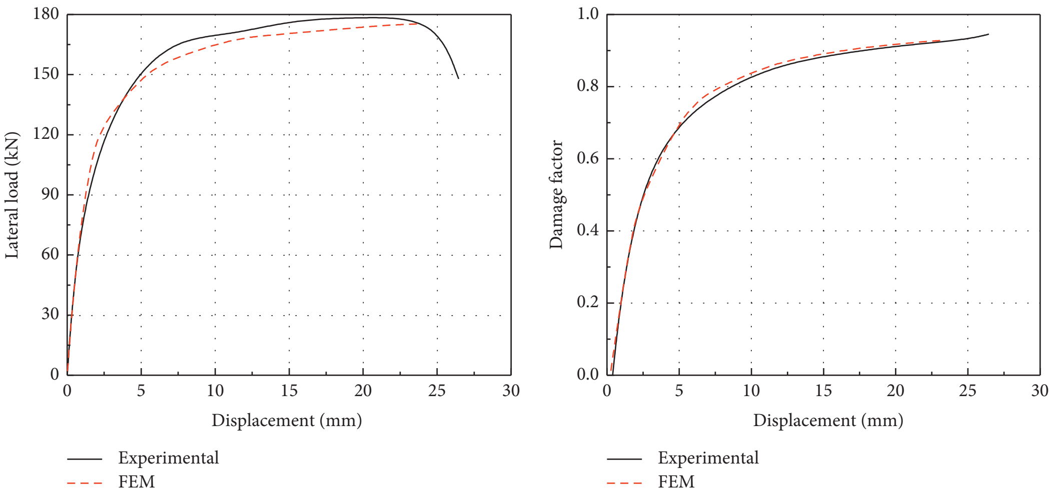

(a)

(b)

Figure 24: Experimental and FEM result comparison of SW2: (a) backbone curves and (b) damage factors.

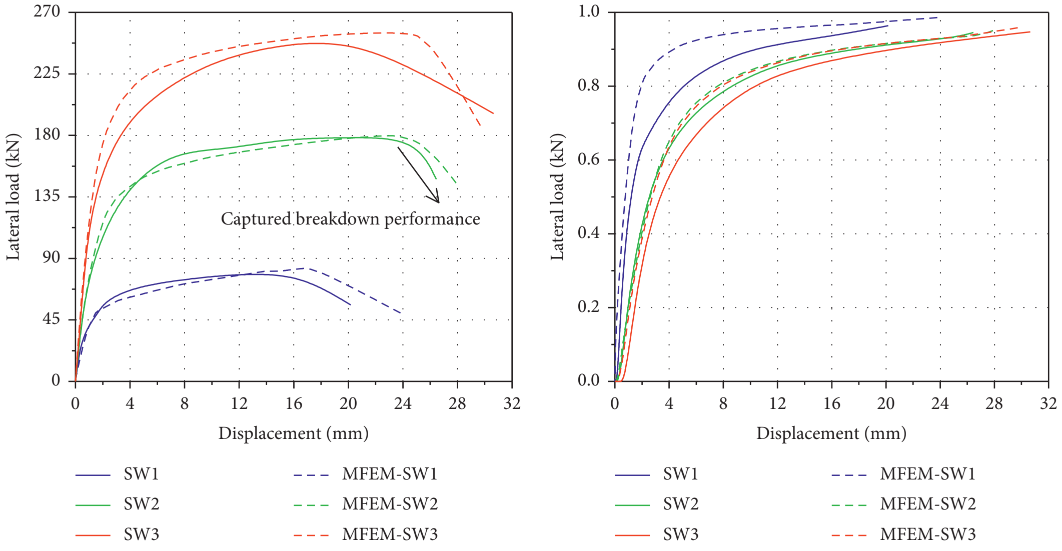

(a)

(b)

Figure 25: Result comparison of the test model and modified FEM (MFEM): (a) backbone curves and (b) damage factors.

Table 4: Comparison of deformations and loads of experiment and MFEM.

Specimen	V_y (kN)	Δ_y (mm)	D_y	V_p (kN)	Δ_p (mm)	D_p	V_u (kN)	Δ_u (mm)	D_u	μ
SW1	62.96	2.99	0.73	78.90	12.35	0.92	67.01	18.33	0.95	6.13
MFEM-SW1	66.34	5.83	0.92	83.52	17.48	0.97	70.99	19.86	0.98	3.41
SW2	149.36	4.62	0.68	178.60	20.08	0.91	151.81	26.25	0.95	5.68
MFEM-SW2	143.56	4.08	0.68	179.98	22.78	0.92	152.98	27.30	0.95	6.69
SW3	203.24	4.86	0.66	249.80	18.72	0.89	212.33	27.75	0.94	5.71
MFEM-SW3	206.74	3.40	0.60	255.43	22.77	0.93	217.12	27.92	0.95	8.21

D_y, D_p, and D_u represent the corresponding damage factors.

5.3. Effect of d. As mentioned above, d is defined as the distance between center of the connection and edge of the shear wall. To investigate the effect of d on the wall performance, MFEMs with various d, including $d = 100$ mm, $d = 150$ mm, $d = 200$ mm, $d = 300$ mm, and $d = 400$ mm, are established and analyzed. The axial compressive ratios are set as 0.1. Figure 27 compares the results of different models. When d increases to 150 mm, the peak load increases to 181.85 kN and ductility factor increases to 7.12. As d increases continually, the peak load

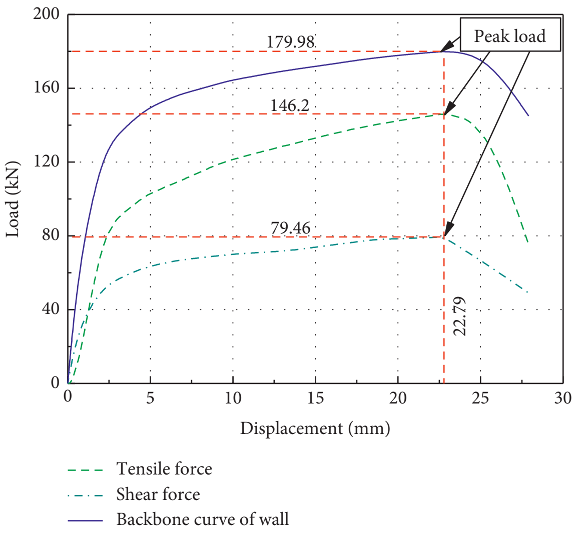

FIGURE 26: Internal force of the connection in MFEM-SW2.

decreases to 176.24 kN, 163.98 kN, and 161.10 kN, respectively, while the corresponding ductility factors are 7.43, 8.3, and 7.0, respectively. The effect of d on the damage factors is slight. At the initial and finial stages, the damage factor curves basically coincide with each other. However, the damage factor of the model with $d = 150$ mm is slightly smaller than other curves at the middle stages. Based on the results, $d = 150$ mm is suggested for the practical use.

6. Simplified Calculation of Lateral Strength

In this section, a simplified calculation method to predict the lateral strength of the precast shear wall is derived for engineering application. According to the failure mode of test specimens, the following assumptions are made to determine the lateral strength of the wall: (a) the failure mode is dominant by axial tension fracture of the connection, and the axial force of connection, T, reaches the axial ultimate load; (b) the contribution of shear deformation of connection to the lateral strength is not taken into account, as well as the interfacial friction; (c) the discrete longitudinal steel bars in the wall are treated as continuum, and the compression zone width is assumed to be the same as that of the concrete compression zone. Therefore, the area of steel bars in the compression zone can be calculated by using equation (4), and the calculation diagram can be simplified and shown in Figure 28. According to the balance of vertical force and bending moment, equations (5) and (6) can be obtained. Then, the lateral strength of the wall, V, can be calculated by solving the equations:

$$A_s = \frac{Ax}{l}, \tag{4}$$

$$N + T = f_c bx + f_y A_s, \tag{5}$$

$$Vh = T\left(l - d - \frac{x}{2}\right) + N\frac{(l - x)}{2}, \tag{6}$$

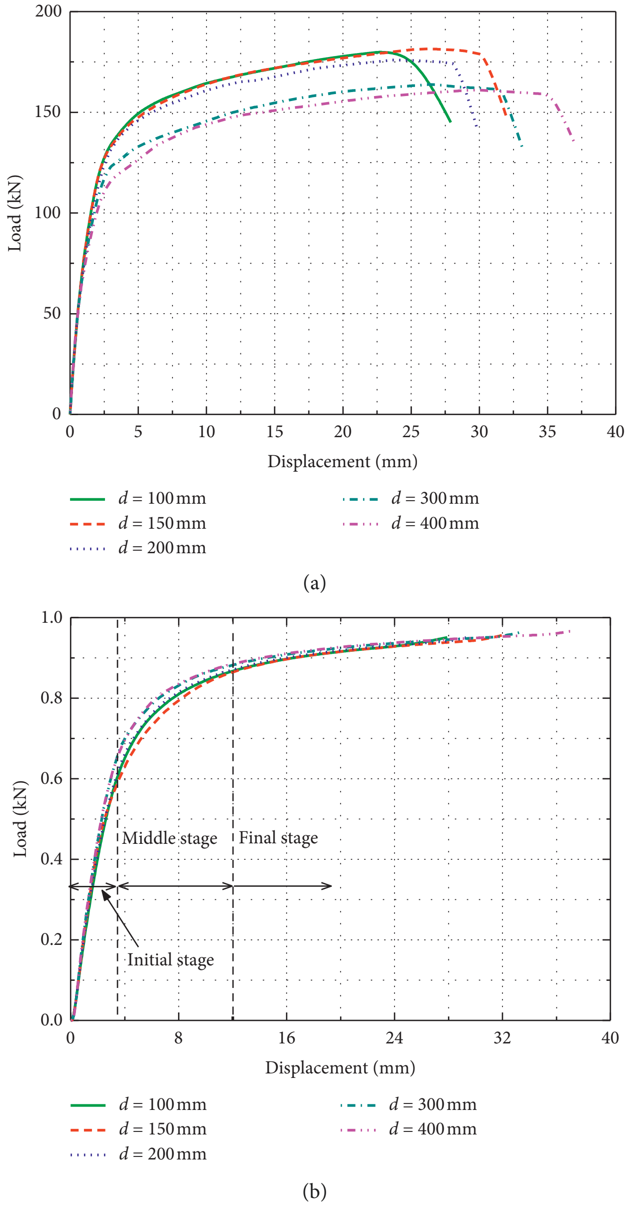

(a)

(b)

FIGURE 27: Result comparison of the models with various d: (a) backbone curves and (b) damage factors.

where A represents the total area of the longitudinal steel bars in the precast wall, x is the width of the compression zone, l is the width of the precast wall, T is the axial strength of connection which can be assumed as 150 kN based on the static test, N represents the axial load, f_c is the compressive strength of concrete, f_y is the yield strength of the steel bars, b is the wall thickness, h is the height of the lateral force, d is the distance between the center of the connection and edge of the shear wall, and V is the lateral strength of the precast wall.

The lateral strength values of walls SW1, SW2, and SW3 are calculated as 78.09 kN, 162.18 kN, and 236.55 kN, respectively. These values well match with the experimental results which are 78.9 kN, 178.6 kN, and 249.8 kN, respectively. To further verify the validation of the simplified method, MFEMs in Section 5.3 is adopted for comparison.

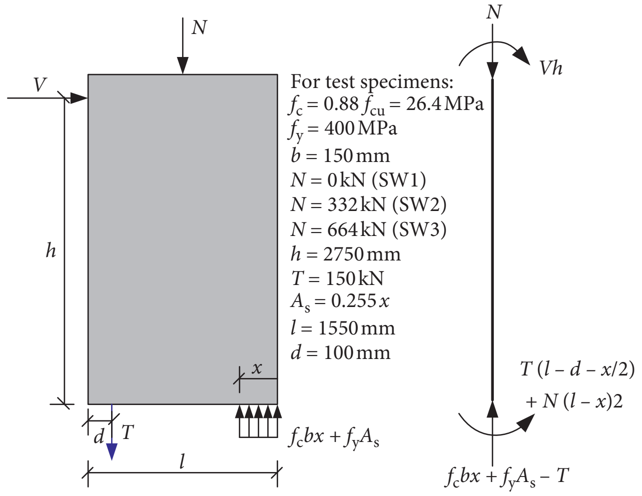

Figure 28: Calculation diagram of the lateral strength.

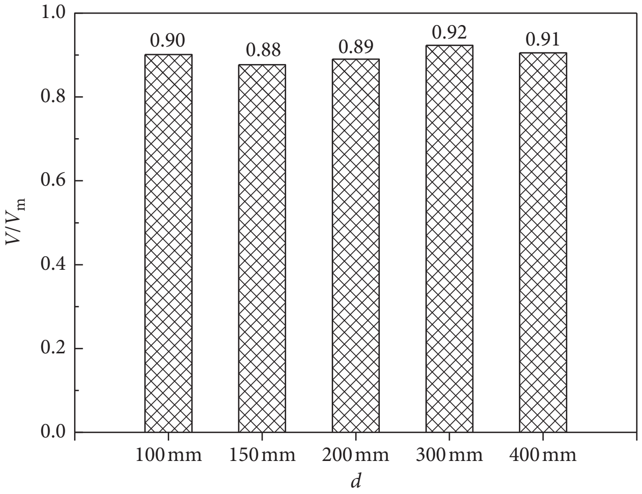

Figure 29: The lateral strength ratios.

The lateral strength ratio which is defined as the ratio of calculation strength V to simulation strength V_m of MFEMs in Section 5.3 is provided in Figure 29. The lateral strength ratios are about 0.9, indicating the accuracy of simplified calculation method again. The calculated strength is more conservative due to the negligence of connection shear deformation and interfacial friction.

Based on the simplified calculation method, the bearing capacity of shear walls under different parameters can be calculated, as listed in Table 5. It can be found that the lateral strength of shear wall increases gradually with the increase of wall thickness, axial compression ratio, and axial strength of connections. In general, the connection strength and axial compression ratio have a greater influence on the lateral strength, while the influence of wall thickness is small. The main reason for this is that the failure mode of precast wall is dominated by connection rupture, not by the complete crushing of concrete. Hence, the wall thickness is recommended to adopt 120 mm or 150 mm in practical engineering applications.

7. Adjusted Collapse Margin Ratio Assessment

Extensive collapse of structure caused by the failure of welded and poorly constructed connection had been reported in the previous studies [21]. It is necessary to evaluate the collapse prevention performance of the low-rise precast wall panel structure system proposed in this paper. Accuracy of the MFEM has been verified on the above. By using the MFEM, an actual three-story structure is numerically established here. The adjusted collapse margin ratio (ACMR) defined in FEMA P695 [31] is used to assess the structural collapse resistance [32]. However, methodology in FEMA P695 needs to perform massive calculation of nonlinear incremental dynamic analysis (IDA), and it is time-consuming. Considering the low-rise precast wall panel structure is first-mode-dominated structure, the ACMR is assessed in this section by using a fast method based on the pushover analysis [33, 34]. This method is essentially a modified version of FEMA P695. It calculates the seismic demand (displacement response here) of earthquake records by the capacity spectrum method, instead of nonlinear time-history analysis.

The three-story precast wall panel structure with dimensions of 9.6 m (length) × 5.1 m (width) × 9 m (height) is simulated. Each story height is 3 m, and the thickness of wall panels is 150 mm. All wall panels are connected by dry connections which have the same design parameters of the cyclic loaded tested specimen in Section 4. Also, the concrete adopts grade C30, and the steel bar adopts HRB400. In total, there are 78 horizontal connections and 48 vertical connections used for the precast wall assembly. The characteristic period of the site is 0.4 s. Peak ground accelerations (PGAs) for the service level earthquake (SLE), design-based earthquake (DBE), and maximum considered earthquake (MCE) are 0.07 g, 0.20 g, and 0.40 g, respectively. The precast shear wall is modeled by using the multilayer shell element. The dry connection is simulated by using the nonlinear zero-length element. Interface contact effect between foundation and wall adopts the friction isolator element. By using the same modeling approach and parameters as the MFEM in Section 5.2, the numerical model of the precast structure is established, as shown in Figure 30.

The first step for the collapse assessment is to perform pushover analysis. The inverted triangle lateral load pattern is applied during the pushover procedure. Figure 31 plots the structure pushover curve and the corresponding idealized bilinear curve. The structure ductility can be calculated as $\mu = 2.58$ according to the bilinear curve. The stiffness hardening after a lateral displacement about 18 mm is caused by the bolt connections because some of which change from the compressive state to the tension state. The fundamental period of the structure is $T_1 = 0.05$ s. The equivalent damping ratio for the elastic design spectrum of Chinese code [22] is adopted approximately as 5% according to the analysis in Section 4.3.2. Then, the elastoplastic demand spectrum for SLE, DBE, and MCE can be given by the elastic design spectrum of Chinese code [20] and Vidic–Fajfar–Fischinger model [35], as shown in Figure 32. It can be observed that seismic capacity can meet the demand of code [22], and the stiffness of the structure is very large. Meanwhile, Figure 33

Table 5: Comparison of shear capacity for different parameters.

Wall thickness, b (mm)	Axial compressive ratio, n	Axial strength of connection, T (kN)	Lateral strength, V_p (kN)
120	0.1	150	159.73
150	0.1	150	162.18
200	0.1	150	164.82
300	0.1	150	167.36
150	01	200	186.36
150	0.1	300	233.82
150	0.1	400	280.45
150	0	150	78.09
150	0.2	150	236.55
150	0.3	150	301.00
150	0.4	150	355.55

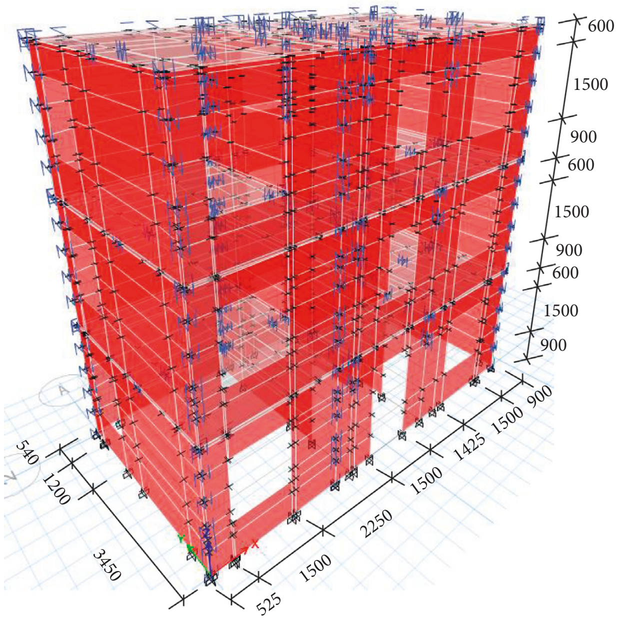

Figure 30: Numerical model of the three-story precast wall panel structure (unit: mm).

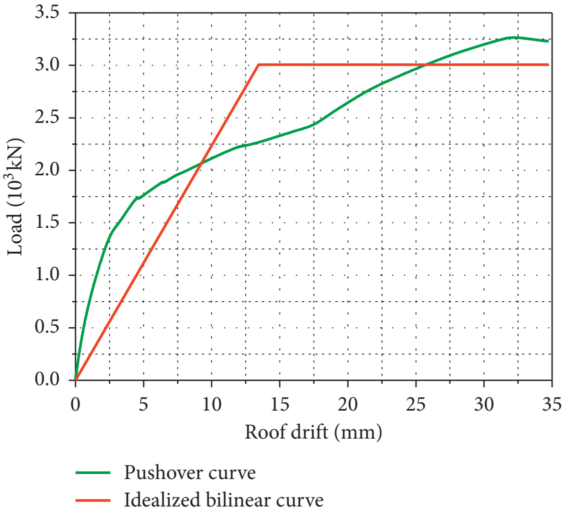

Figure 31: Pushover curve.

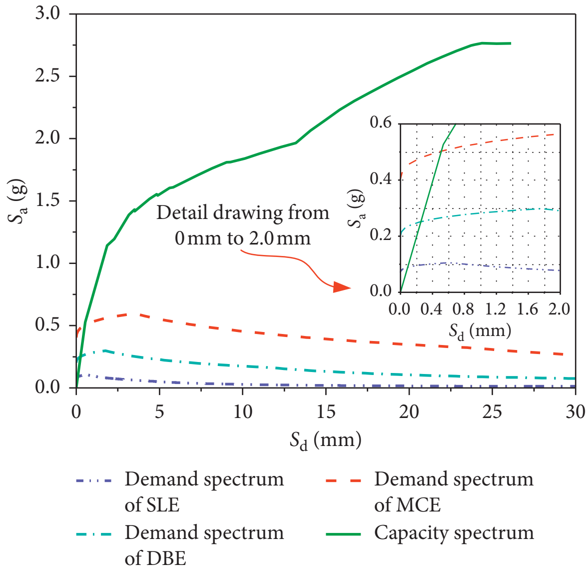

Figure 32: Capacity and elastoplastic demand spectrum.

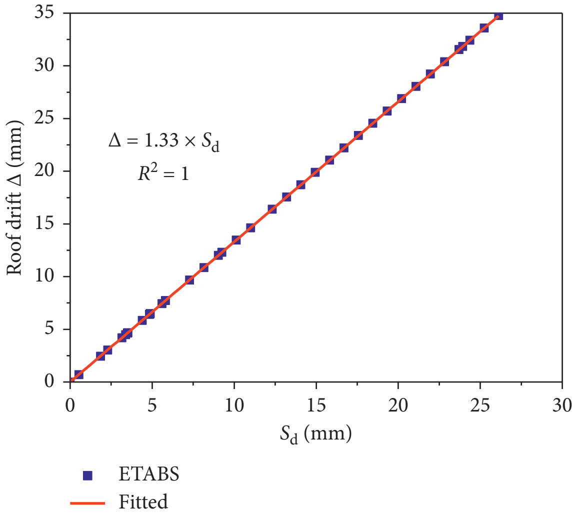

Figure 33: Relationship of the roof drift and S_d.

provides the relationship between roof drift and spectral displacement S_d. The results show that 1.33 can be used as the coefficient to modify the spectral displacement of equivalent linear single degree-of-freedom (ELSDOF) system to roof drift of multiple DOF system. It verifies rationality of ASCE/SEI 41-06 [36] which suggested the modified coefficient as 1.3.

The next step is to obtain the structural performance curves based on the pushover results. Firstly, 16 ground motions are selected, as listed in Table 6, and the comparison of response spectra is plotted in Figure 34. Secondly, the intensity of each record is scaled incrementally from 50% to 1200% of the MCE intensity. And the elastoplastic demand spectrum of each record should be calculated using the method mentioned above. Thirdly, the target S_d can be obtained from the intersection point between the capacity spectrum of the structure and elastoplastic demand spectrum of the records. Then target S_d is multiplied by 1.33 to get the roof drift of the precast wall panel structure (Figure 33). Taking this calculation process for different intensities of each seismic record, the performance curves can be obtained then, as drawn in Figure 35.

The third step is to develop collapse fragility curve based on performance curves. The development employs the fitting technique proposed by Porter [34]. In Section 4.3.3, the damage factor, 0.90, is suggested for collapse prevention. Moreover, the damage factor at the peak load point of the pushover curve (Figure 32) is calculated as 0.9. Thus, for each individual performance curve, spectral acceleration at which the damage factor exceeds 0.9 is defined as the state of structural collapse. According to the secant stiffness of each performance curve and equation (3), the spectral acceleration of each record corresponding to structural collapse can be obtained, as listed in Table 7. According to Porter [37], the fragility parameters can be computed as

$$x_\mathrm{m} = \exp\left(\frac{1}{N}\sum_{i=1}^{N}\ln r_i\right),$$

$$\beta = \sqrt{\frac{1}{N-1}\sum_{i=1}^{N}\left(\ln\frac{r_i}{x_\mathrm{m}}\right)^2 + \beta_u^2} = \sqrt{\beta_\mathrm{fit}^2 + \beta_\mathrm{u}^2}, \tag{7}$$

where N is the number of records, r_i is the spectral acceleration at which the structural is collapsed in i-th records, and β_u equals to 0.25 due to all specimens were under the same configuration [37]. The developed collapse fragility curve is shown in Figure 36. The median collapse spectral acceleration S_CT can be obtained from the curve as 4.28 g. At the structural fundamental period, the median MCE, S_MT, is 0.65 g. Hence, the collapse margin ratio (CMR), which is defined as the ratio of S_CT to S_MT, is calculated as 6.58 for the precast wall panel structure.

The final step is to determine the structural ACMR by adjusting the CMR with a spectral shape factor (SSF). It can be expressed as

$$\mathrm{ACMR} = \mathrm{SSF} \times \mathrm{CMR} = \mathrm{SSF} \times \frac{S_\mathrm{CT}}{S_\mathrm{MT}}. \tag{8}$$

The SSF in this case can be calculated to be 1.17 based on the structural fundamental period and ductility [27].

Table 6: Earthquake records.

No.	Event	Year	Magnitude	NGA#	Record
1	San Fernando	1971	6.61	57	ORR021
2	San Fernando	1971	6.61	83	PUD055
3	Imperial Valley-06	1979	6.53	175	E12140
4	Imperial Valley-06	1979	6.53	167	CMP015
5	Superstition Hills-01	1987	6.2	718	IVW090
6	Superstition Hills-01	1987	6.2	726	WLF225
7	Loma_Prieta	1989	6.9	762	FRE000
8	Loma_Prieta	1989	6.9	800	SJW160
9	Landers	1992	7.28	850	DSP000
10	Landers	1992	7.28	3757	NPF090
11	Northridge-01	1994	6.69	970	FAI095
12	Northridge-01	1994	6.69	1000	PIC090
13	Kobe-Japan	1995	6.9	1100	ABN000
14	Kobe-Japan	1995	6.9	1102	CHY000
15	Chi-Chi_Taiwan-05	1999	6.2	3160	TCU014 N
16	Chi-Chi_Taiwan-05	1999	6.2	3191	TCU081 N

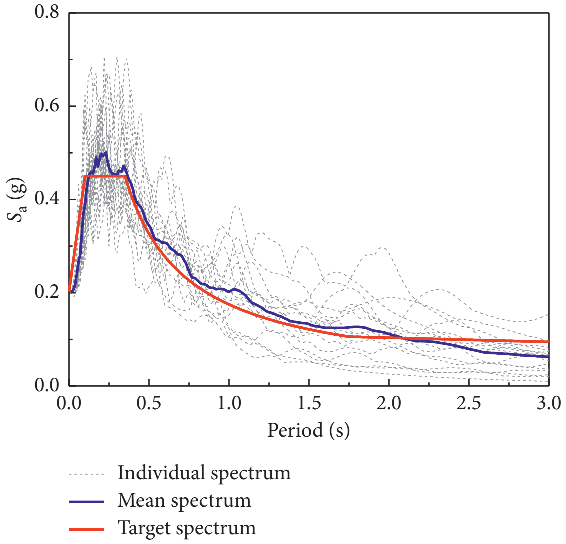

Figure 34: Response spectrum of earthquake records scaled to DBE.

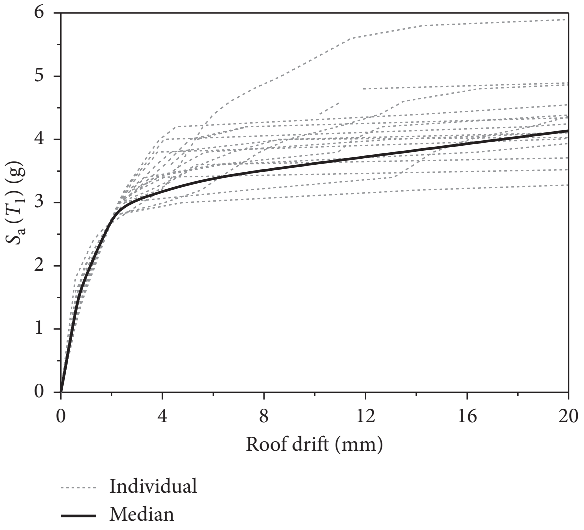

Figure 35: Performance curves based on pushover analysis.

Table 7: Spectral accelerations of the structural collapse.

Earthquake no.	S_a (T_1) (g)	Earthquake no.	S_a (T_1) (g)	Earthquake no.	S_a (T_1) (g)	Earthquake no.	S_a (T_1) (g)
1	4.96	5	4.36	9	4.15	13	5.05
2	4.15	6	4.94	10	4.20	14	5.90
3	4.45	7	3.76	11	4.12	15	3.58
4	3.2	8	3.92	12	3.99	16	4.42

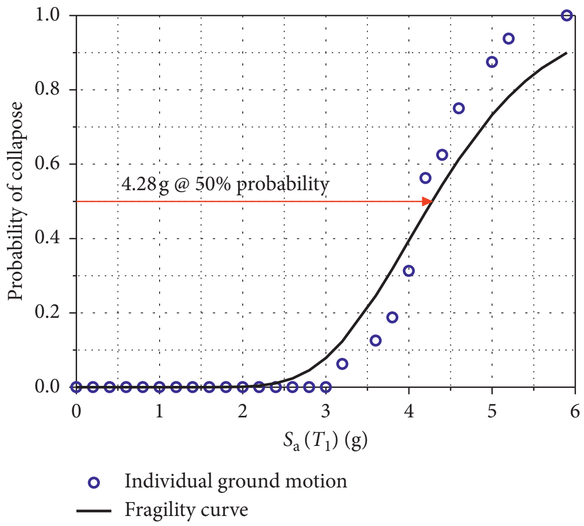

Figure 36: Collapse fragility curve of the structure.

Hence, ACMR for the proposed precast wall panel structure is computed as 7.70. For ACMR assessment, it needs to determine the acceptable value of ACMR based on the total system collapse uncertainty β_{TOT}. This uncertainty is due to the record-to-record variability in the ground motions β_{RTR}, the quality ratings of design requirement β_{DR}, test data β_{TD}, and numerical model β_{MDL}. β_{TOT} can be obtained as

$$\beta_{\mathrm{TOT}} = \sqrt{\beta_{\mathrm{RTR}}^2 + \beta_{\mathrm{DR}}^2 + \beta_{\mathrm{TD}}^2 + \beta_{\mathrm{MDL}}^2}. \quad (9)$$

In this case, β_{TOT} is computed to be 0.65 according to FEMA P695 [31]. And the acceptable ACMRs for a collapse probability of 10% and 20% are 2.30 and 1.73, respectively [31]. The result shows that the proposed structure with an AMCR of 7.70 has high seismic resistance against collapse during strong earthquake excitations.

8. Conclusions

A novel type of dry connection is presented and the corresponding low-rise precast wall panel structure system was introduced in this study. To assess the seismic performance of the connection and structure system, experimental work and numerical analyses are conducted. Based on the test and simulation, the following conclusions can be obtained:

(1) Failure mode of the connection in axial tensile loading follows the sequence of anchored rebar slipping, concrete cracking, steel plate bending, and anchored rebar rupturing. In the shear loading, it generally follows the sequence of the bolt slipping, concrete cracking, and anchor rebar rupturing. The connection has a good ductile behavior. Moreover, axial and shear mechanical models of the connection are provided by the test results.

(2) Failure mode of the precast shear wall includes the concrete crushing and connection rupturing, which is mainly induced by flexural stress. Test shows that the precast system has a stable energy dissipation capacity and a satisfactory seismic ductility with minimum average ductility factor of 4.97 and small residual displacement. Meanwhile, the damage factor, which is defined based on secant stiffness, is suggested to be 0.90 for the performance state of collapse prevention.

(3) Numerical analysis modified by using the tested shear wall shows a good nonlinear behavior of the proposed wall panel system. Then, a simplified calculation method to predict the lateral strength of the precast shear wall is derived, and the accuracy is verified.

(4) The distance between center of the connection and edge of the shear wall, *d*, is suggested to be 150 mm, and the wall thickness, *b*, is recommended to be 120 mm or 150 mm in practical engineering.

(5) Adjusted collapse margin ratio (AMCR) of three-story precast wall panel structure systems is calculated to be 7.70, indicating the presented structure system has high seismic resistance against collapse in the strong earthquakes.

Data Availability

The data used to support the findings of this study are included within the article.

Disclosure

Any opinions, findings, and conclusions or recommendations expressed in this paper are those of the authors.

Conflicts of Interest

The authors declare that they have no conflicts of interest.

Acknowledgments

The authors are grateful for the financial support from the Fundamental Research Funds for the Central Universities of the Central South University (project no. 502221804), National Natural Science Foundation of China (Project no. 51878674), Foundation for Key Youth Scholars in Hunan Province, and Project of Yuying Plan in Central South University.

References

[1] G. Xu, Z. Wang, B. Wu et al., "Seismic performance of precast shear wall with sleeves connection based on experimental and numerical studies," *Engineering Structures*, vol. 150, pp. 346–358, 2017.

[2] E. Brunesi, R. Nascimbene, and A. Pavese, "Mechanical model for seismic response assessment of lightly reinforced concrete walls," *Earthquakes and Structures*, vol. 11, no. 3, pp. 461–481, 2016.

[3] E. Brunesi and R. Nascimbene, "Experimental and numerical investigation of the seismic response of precast wall connections," *Bulletin of Earthquake Engineering*, vol. 15, no. 12, pp. 5511–5550, 2017.

[4] D. Guan, C. Jiang, Z. Guo, and H. Ge, "Development and seismic behavior of precast concrete beam-to-column connections," *Journal of Earthquake Engineering*, vol. 22, no. 2, pp. 234–256, 2018.

[5] Z. Zhu and Z. Guo, "In-plane quasi-static cyclic tests on emulative precast concrete walls," *KSCE Journal of Civil Engineering*, vol. 22, no. 8, pp. 2890–2898, 2018.

[6] Z. Zhu and Z. Guo, "Experimental study on emulative hybrid precast concrete shear walls," *KSCE Journal of Civil Engineering*, vol. 21, no. 1, pp. 329–338, 2017.

[7] M. R. Song, J. X. He, Y. Liu et al., "Seismic behavior of three-story prestressed fabricated concrete frame under dynamic and low reversed cyclic loading," *Advances in Civil Engineering*, vol. 2018, Article ID 7876908, 10 pages, 2018.

[8] L. Segura-Castillo, N. García, I. R. Viacava, and G. R. de Sensale, "Structural model for fibre-reinforced precast concrete sandwich panels," *Advances in Civil Engineering*, vol. 2018, Article ID 3235012, 11 pages, 2018.

[9] R. Shahi, N. Lam, E. Gad, J. Wilson, and K. Watson, "Seismic performance behavior of cold-formed steel wall panels by quasi-static tests and incremental dynamic analyses," *Journal of Earthquake Engineering*, vol. 21, no. 3, pp. 411–438, 2017.

[10] W. Y. Lim, H. K. Kang, and S. G. Hong, "Cyclic lateral testing of precast concrete T-walls in fast low-rise construction," *ACI Structural Journal*, vol. 113, no. 1, pp. 179–189, 2016.

[11] D. Wu, S. Liang, Z. Guo, X. Zhu, and Q. Fu, "The development and experimental test of a new pore-forming grouted precast shear wall connector," *KSCE Journal of Civil Engineering*, vol. 20, no. 4, pp. 1462–1472, 2016.

[12] A. Pavese and D. A. Bournas, "Experimental assessment of the seismic performance of a prefabricated concrete structural wall system," *Engineering Structures*, vol. 33, no. 6, pp. 2049–2062, 2011.

[13] C. Todut, D. Dan, and V. Stoian, "Theoretical and experimental study on precast reinforced concrete wall panels subjected to shear force," *Engineering Structures*, vol. 80, pp. 323–338, 2014.

[14] S. Gavridou, "Shake table testing and analytical modeling of a full-scale four-story unbonded post-tensioned concrete wall building," Dissertations and Theses-Gradworks, University of California, Los Angeles, CA, USA, 2015.

[15] A. Akin and R. Sezer, "A study on strengthening of reinforced concrete frames using precast concrete panels," *KSCE Journal of Civil Engineering*, vol. 20, no. 6, pp. 2439–2446, 2016.

[16] B. D. Lago, F. Biondini, and G. Toniolo, "Friction-based dissipative devices for precast concrete panels," *Engineering Structures*, vol. 147, pp. 356–371, 2017.

[17] T. Guo, G. Zhang, and C. Chen, "Experimental study on self-centering concrete wall with distributed friction devices," *Journal of Earthquake Engineering*, vol. 18, no. 2, pp. 214–230, 2014.

[18] D. A. Bournas, P. Negro, and F. J. Molina, "Pseudodynamic tests on a full-scale 3-storey precast concrete building: behavior of the mechanical connections and floor diaphragms," *Engineering Structures*, vol. 57, no. 4, pp. 609–627, 2013.

[19] C. Bora, M. G. Oliva, S. D. Nakaki, and R. Becker, "Development of a precast concrete shear-wall system requiring special code acceptance," *PCI Journal*, vol. 52, no. 1, pp. 122–135, 2007.

[20] J. Sun, H. Qiu, and H. Jiang, "Experimental study and associated mechanism analysis of horizontal bolted connections involved in a precast concrete shear wall system," *Structural Concrete*, vol. 20, no. 1, pp. 282–295, 2019.

[21] EERI, "Armenia earthquake reconnaissance report," in *Earthquake Spectra*, p. 175, Earthquake Engineering Research Institute (EERI), Oakland, CA, USA, 1989.

[22] GB 50011-2010, *Code for Seismic Design of Buildings*, China Architecture and Industry Press, Beijing, China, 2010, in Chinese.

[23] ASCE, *Minimum Design Loads for Buildings and Other Structures (ASCE/SEI 7-10)*, American Society of Civil Engineers (ASCE), Reston, VA, USA, 2014.

[24] W. Guo, Z. Zhai, Y. Cui, Z. Yu, and X. Wu, "Seismic performance assessment of low-rise precast wall panel structure with bolt connections," *Engineering Structures*, vol. 181, pp. 562–578, 2019.

[25] GB 50017-2003, *Code for Design of Steel Structures*, China Architecture and Industry Press, Beijing, China, 2003, in Chinese.

[26] JGJ 101-96, *Specificating of Testing Methods for Earthquake Resistant Building*, China Architecture and Industry Press, Beijing, China, 1997, in Chinese.

[27] A. K. Chopra, *Dynamics of Structures*, Prentice-Hall, Upper Saddle River, NJ, USA, 1981.

[28] N. Mendes, P. B. Lourenço, and A. Campos-Costa, "Shaking table testing of an existing masonry building: assessment and improvement of the seismic performance," *Earthquake Engineering & Structural Dynamics*, vol. 43, no. 2, pp. 247–266, 2014.

[29] X. Lu, L. Xie, H. Guan, Y. Huang, and X. Lu, "A shear wall element for nonlinear seismic analysis of super-tall buildings using OpenSees," *Finite Elements in Analysis and Design*, vol. 98, pp. 14–25, 2015.

[30] GB 50010-2010, *Code for Design of Concrete Structures*, China Architecture and Industry Press, Beijing, China, 2010, in Chinese.

[31] FEMA P695, *Quantification of Building Seismic Performance Factors*, Federal Emergency Management Agency, Washington, DC, USA, 2009.

[32] T. Guo, L.-L. Song, and G.-D. Zhang, "Numerical simulation and seismic fragility analysis of a self-centering steel MRF with web friction devices," *Journal of Earthquake Engineering*, vol. 19, no. 5, pp. 731–751, 2015.

[33] A. Azarbakht and M. Dolšek, "Progressive incremental dynamic analysis for first-mode dominated structures," *Journal of Structural Engineering*, vol. 137, no. 3, pp. 445–455, 2011.

[34] D. Vamvatsikos and C. Allin Cornell, "Direct estimation of the seismic demand and capacity of oscillators with multi-linear

static pushovers through IDA," *Earthquake Engineering & Structural Dynamics*, vol. 35, no. 9, pp. 1097–1117, 2006.

[35] T. Vidic, P. Fajfar, and M. Fischinger, "Consistent inelastic design spectra: strength and displacement," *Earthquake Engineering & Structural Dynamics*, vol. 23, no. 5, pp. 507–521, 1994.

[36] ASCE/SEI 41-06, *Seismic Evaluation and Retrofit of Existing Buildings*, American Society of Civil Engineers, Reston, VA, USA, 2006.

[37] K. Porter, R. Kennedy, and R. Bachman, *Developing Fragility Functions for Building Components for ATC-58. A Report to ATC-58*, Applied Technology Council, Redwood City, CA, USA, 2006.